Design and Evaluation of Medium Speed Geared Direct Grid-Connected Wind Generator Drive Train with Specific Focus on Slip Permanent Magnet Coupling

by

Petrus Johannes Jacobus van Wyk

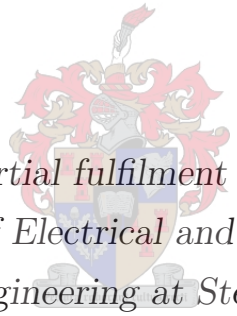

Thesis presented in partial fulfilment of the requirements for the degree of Master of Electrical and Electronic Engineering in the Faculty of Engineering at Stellenbosch University

Department of Electric and Electronic Engineering,
Stellenbosch University,
Private Bag X1, Matieland 7602, South Africa.

Supervisor: Prof. M.J. Kamper

December 2015

Declaration

By submitting this thesis electronically, I declare that the entirety of the work contained therein is my own, original work, that I am the sole author thereof (save to the extent explicitly otherwise stated), that reproduction and publication thereof by Stellenbosch University will not infringe any third party rights and that I have not previously in its entirety or in part submitted it for obtaining any qualification.

December 2015

Abstract

Design and Evaluation of Medium Speed Geared Direct Grid-Connected Wind Generator Drive Train with Specific Focus on Slip Permanent Magnet Coupling

P.J.J. van Wyk

Department of Electric and Electronic Engineering,
Stellenbosch University,
Private Bag X1, Matieland 7602, South Africa.

Thesis: M.Eng (EE)

December 2015

In this study an alternative drive train topology for the slip-synchronous permanent magnet generator (SS-PMG) is proposed. The SS-PMG was first proposed in 2010 and is a direct drive, direct grid-connected wind generator, consisting of two sections, a slip permanent magnet coupling (S-PMC) and a permanent magnet synchronous generator (PMSG). These two machines are mechanically connected via a common PM rotor. The PMSG section is directly grid-connected, but this is only possible due to the damping effects of the S-PMC on wind transients. Since the SS-PMG is a direct drive generator, it operates at turbine speed.

In this thesis it is proposed that the SS-PMG be split into two separate machines: a free standing S-PMC and a free standing PMSG. It is also proposed that a gearbox be introduced, to allow greater flexibility in speed selection, which allows the S-PMC and PMSG to operate in the medium speed range (100 - 600 r/min) or at even higher speeds for small scale turbines.

All the components of the drive train are investigated. The turbine blade characteristics are combined with the wind speed data of a proposed wind

site to determine the drive train operating speed, as well as the S-PMC and PMSG power ratings. The gearbox is investigated and laboratory tested to determine its operating efficiency. A free standing S-PMC is not widely known in literature, and thus the S-PMC is investigated in great detail. The S-PMC is simulated and design optimised using finite element (FE) modelling, and a 2.2 kW prototype of the S-PMC is built and laboratory tested. The PMSG is also simulated and design optimised using FE modelling, but a prototype was not built. Finally the efficiency of the entire drive train is evaluated, by combining measured, simulated and calculated data of the various drive train components.

The gearbox achieves a high efficiency of up to 96% at rated loads. The S-PMC performs better than expected, with the prototype producing 20% more output torque than the S-PMC simulations at rated slip, due to superior thermal characteristics of the open design. The proposed FE analysis method for the S-PMC proves to accurately model the machine. The simulated PMSG achieves a 93% efficiency at rated conditions and appears to be feasible for direct grid-connected use. The entire drive train shows to have a good efficiency of above 80% for most of its operating range.

Uittreksel

Ontwerp en Evaluasie van Medium Spoed Geratde Direk Netwerk Gekoppelde Wind Generator Aandryfstelsel met Spesifieke Fokus op Glip Permanente Magneet Koppeling

("Design and Evaluation of Medium Speed Geared Direct Grid-Connected Wind Generator Drive Train with Specific Focus on Slip Permanent Magnet Coupling")

P.J.J. van Wyk

Departement Elektries en Elektroniese Ingenieurswese,
Stellenbosch Universiteit,
Privaatsak X1, Matieland 7602, Suid Afrika.

Tesis: M.Ing (EE)

Desember 2015

In hierdie studie word 'n alternatiewe aandrywingstelsel topologie vir die glip-sinchroon permanente magneet generator (SS-PMG) voorgestel. Die SS-PMG is die eerste keer voorgestel in 2010 en is 'n direk aangedrewe, direk netwerk gekoppelde wind generator, wat bestaan uit twee gedeeltes, 'n glip permanente magneet koppeling (S-PMC) en 'n permanente magneet sinchroon generator (PMSG). Hierdie twee masjiene word meganies verbind deur 'n gemeenskaplike PM rotor. Die PMSG is direk netwerk gekoppel, maar dit is slegs moontlik weens die dempingseffek van die S-PMC op wind oorgangsverskynsels. Aangesien die SS-PMG 'n direk aangedrewe generator is, hardloop dit teen turbine spoed.

In hierdie tesis word dit voorgestel dat die SS-PMG verdeel word in twee afsonderlike masjiene: 'n vrystaande S-PMC en 'n vrystaande PMSG. Dit word ook voorgestel dat 'n ratkas bygevoeg word, om meer vryheid te gee met spoed seleksie, wat die S-PMC en PMSG toelaat om te werk in die medium spoed

reeks (100-600 r/min), of moontlik teen selfs hoër snelhede vir kleinskaalse turbines.

Al die komponente van die aandryfstelsel word ondersoek. Die turbine lem eienskappe word gekombineer met wind spoed data van 'n voorgestelde wind plaas om die aandryfstelsel spoed te bepaal, sowel as om die S-PMC en PMSG drywing groottes te bepaal. Die ratkas word ondersoek en in die laboratorium getoets om sy bedryfseffektiwiteit te bepaal. 'n Vrystaande S-PMC is nie wyd bekend in die literatuur nie, en dus word die S-PMC in groot detail ondersoek. Die S-PMC word gesimuleer en ontwerp met behulp van eindige element (FE) modellering, en 'n 2.2 kW prototipe van die S-PMC word gebou en in die laboratorium getoets. Die PMSG word ook gesimuleer en ontwerp met behulp van FE modellering, maar 'n prototipe was nie gebou. Ten slotte word die effektiwiteit van die hele aandryfstelsel geëvalueer met 'n kombinasie van gemete, gesimuleerde en berekende data van die verskillende aandryfstelsel komponente.

Die ratkas bereik 'n hoë effektiwiteit van tot 96% by kenlas. Die S-PMC presteer beter as te verwagte, met die prototipe wat teen kenglip 20% meer wringkrag uitsit as die S-PMC simulasies, te danke aan beter termiese eienskappe weens die oop ontwerp. Dit word bevind dat die voorgestelde FE analise metode vir die S-PMC die masjien akkuraat modelleer. Die gesimuleerde PMSG bereik 'n effektiwiteit van 93% teen kenwaardes en blyk om bruikbaar te wees vir 'n direk netwerk gekoppelde toepassing. Dit word bevind dat die hele aandryfstelsel 'n goeie effektiwiteit van bo 80% het vir die meerderheid van sy reeks bedryfspunte.

Acknowledgements

I would like to express my sincere gratitude to the following people and organisations:

My promoter Prof. Maarten Kamper, for his guidance and valuable input throughout the course of this study.

The National Research Foundation (NRF) for financial support during the study.

Armin Henning for his many hours of assistance with prototype construction, and test bench design and construction.

Reynold Kleinsmidt and David Groenewald for help with prototype and test bench design and construction.

André Swart, Murray Jumat and Pietro Petzer from the SED workshop, for all their assistance.

Everyone in the Electrical Machines Laboratory, for invaluable assistance, insightful conversations and a very memorable experience.

Contents

List of Figures

List of Tables

Nomenclature

Variables

a	Dimensional variable	[mm]
A	Swept area of wind turbine	[m^2]
A_{co}	Active conductor area of slot	[mm^2]
b	Dimensional variable	[mm]
B_{mt}	Maximum flux density in stator teeth	[T]
B_{my}	Maximum flux density in stator yoke	[T]
c	Dimensional variable	[mm]
c_s	Coil span	[ ]
C	Core loss equation constant	[ ]
C_p	Coefficient of wind power	[ ]
d_i	Stator inner diameter	[m]
E_a	Internally generated voltage (EMF), RMS	[V]
f	Frequency	[Hz]
h_c	Coil height	[mm]
h_m	Magnet height	[mm]
h_{pmy}	PM rotor yoke height	[mm]
h_y	Rotor yoke height	[mm]
h_{ry}	Wound rotor yoke height	[mm]
h_t	Tooth height	[mm]
$\mathbf{I}_{abc}$	Three-phase current matrix (ABC)	[A]
$\mathbf{I}_{abc(i)}$	Three-phase current matrix (ABC, ith set)	[A]
I_{di}	Wound rotor direct axis current (ith set)	[A]
$\mathbf{I}_{dq}$	dq current matrix	[A]

$\mathbf{I}_{\mathrm{dq}(i)}$	dq current matrix (ith set)	[A]
I_{ds}	Stator direct axis current	[A]
$I_{\mathrm{q}i}$	Wound rotor quadrature axis current (ith set)	[A]
I_{qs}	Stator quadrature axis current	[A]
$I_{\mathrm{RMS}i}$	Wound rotor RMS phase current (ith set)	[A]
I_{s}	Stator current	[A]
k	Weibull shape parameter	[ ]
k_1	End winding inductance constant	[ ]
k_2	End winding inductance constant	[ ]
k_{d}	Standard distribution factor	[ ]
$k_{\mathrm{e}(p)}$	End winding factor	[ ]
$k_{\mathrm{p(u)}}$	End winding pitch factor	[ ]
K	End winding inductance constant	[ ]
$\mathbf{K}_{\mathrm{p}}$	Park's transformation	[ ]
l	Stack length	[mm]
l_{a}	Axial/stack length	[mm]
l_{e}	Length of end winding	[mm]
l_{g}	Length of gap between stack and end winding	[mm]
$L_{\mathrm{d}i}$	Wound rotor direct axis inductance (ith set)	[H]
L_{ds}	Stator direct axis inductance	[H]
L_{e}	Per phase end winding inductance	[H]
$L_{\mathrm{e}i}$	Wound rotor per phase end winding inductance (ith set)	[H]
L_{es}	Stator per phase end winding inductance	[H]
$L_{\mathrm{q}i}$	Wound rotor quadrature axis inductance (ith set)	[H]
L_{qs}	Stator quadrature axis inductance	[H]
m	Mass of air	[kg]
M_{t}	Mass of stator teeth	[kg]
M_{y}	Mass of stator yoke	[kg]
n_{a}	Number of parallel circuits	[ ]
N_{c}	Number of turns per coil	[ ]
N_{in}	Input mechanical speed	[r/min]

N_{out}	Output mechanical speed	[r/min]
N_{ph}	Number of phases	[ ]
N_{sync}	Synchronous mechanical speed	[r/min]
p	Number of poles	[ ]
P_{c}	Core losses	[W]
P_{co}	Wound rotor conductor losses	[W]
P_{cus}	Stator copper losses	[W]
P_{fw}	Friction and windage losses	[W]
P_{in}	Input power	[W]
P_{losses}	Power losses	[W]
P_{m}	Extracted mechanical wind power	[W]
P_{mech}	Mechnical power	[W]
P_{out}	Output power	[W]
P_{w}	Available wind power	[W]
q	Number of slots per pole per phase	[ ]
q_{c}	Number of coils per phase	[ ]
q_{ph}	Number of spokes per phase	[ ]
Q	Number of slots	[ ]
r_{c}	Average coil radius	[mm]
r_{in}	Inside radius	[mm]
r_{out}	Outside radius	[mm]
R	Radius of rotor swept area	[m]
R_{c}	Core resistance	[Ω]
R_{r}	Rotor per phase winding resistance	[Ω]
R_i	Wound rotor per phase winding resistance (ith set)	[Ω]
R_{s}	Stator per phase winding resistance	[Ω]
s	Slip	[ ]
S	Apparant power	[VA]
t	Machine periodicity	[ ]
t_{c}	Conductor temperature	[°C]
T	Generated torque	[Nm]

T_{in}	Input torque	[Nm]
T_{rated}	Rated torque	[Nm]
v	Wind speed	[m/s]
V_{ds}	Stator direct axis phase voltage	[V]
V_{qs}	Stator quadrature axis phase voltage	[V]
V_{s}	Stator phase voltage	[V]
$V_{(\text{u})}$	End winding shape factor	[ ]
w_{c}	Coil width	[mm]
w_{s}	Slot width	[mm]
w_{sg}	Slot width	[mm]
w_{t}	Tooth width	[mm]
W	Number of turns in series per phase	[ ]
x	Core loss equation constant	[ ]
y	Core loss equation constant	[ ]
Y_{t}	Thermal coefficient of conductor	[K^{-1}]
z	Number of conductors per slot	[ ]
α	Angle between phase A axis and direct axis	[rad]
α_{ph}	Angle between spokes	[degrees]
β	Dimentional ratio	[ ]
δ	Slot-pitch angle (electrical)	[degrees]
Δ	Voltage angle	[rad]
η	Efficiency	[%]
η_{gb}	Gearbox efficiency	[%]
θ	Power factor angle	[degrees]
θ_i	Angle between d-axis and phase A axis (ith set)	[degrees]
λ	Weibull scale parameter	[ ]
$\boldsymbol{\lambda}_{\text{abc}}$	Three phase flux linkage matrix	[Wb·turn]
$\boldsymbol{\lambda}_{\text{abc}(i)}$	Three phase flux linkage matrix (ith set)	[Wb·turn]
$\lambda_{\text{d}i}$	Wound rotor direct axis flux linkage (ith set)	[Wb·turn]
$\boldsymbol{\lambda}_{\text{dq}}$	dq flux linkage matrix	[Wb·turn]
$\boldsymbol{\lambda}_{\text{dq}(i)}$	dq flux linkage matrix (ith set)	[Wb·turn]

λ_{ds}	Stator direct axis flux linkage	[Wb·turn]
λ_{qi}	Wound rotor quadrature axis flux linkage (ith set)	[Wb·turn]
λ_{qs}	Stator quadrature axis flux linkage	[Wb·turn]
λ_{mi}	PM flux linkage contribution on wound rotor (ith set)	[Wb·turn]
λ_{ms}	PM flux linkage contribution on stator	[Wb·turn]
ϕ	Current angle	[rad]
ρ	Density of air	[kg/m^3]
ρ_m	Magnet pitch	[%]
ρ_t	Resistivity of conductor	[Ω·m]
ω	Turbine rotor speed (mechanical)	[rad/s]
ω_{in}	Input speed (mechanical)	[rad/s]
ω_s	Synchronous speed (electrical)	[rad/s]
ω_{sl}	Slip speed (mechanical)	[rad/s]
ω_{sle}	Slip speed (electrical)	[rad/s]
ω_m	PM rotor angular speed (electrical)	[rad/s]
ω_r	Wound rotor angular speed (electrical)	[rad/s]

Subscripts

d	Direct axis
e	End winding
gb	Gearbox
i	Slip coupler winding set number
m	Permanent magnet
q	Quadrature axis
r	Rotor
s	Stator
t	Tooth
u	Winding shape
y	Yoke

Abbreviations

CAD	Computer aided design
CF	Capacity factor
DC	Direct current
DFIG	Doubly fed induction generator
FE	Finite element
FEM	Finite element method
GCC	Grid connection controller
IACS	International Annealed Copper Standard
IG	Induction generator
IM	Induction motor
MMFD	Modified method of feasible direction
PM	Permanent magnet
PMIG	Permanent magnet induction generator
PMSG	Permanent magnet synchronous generator
RMS	Root mean square
SEMFEM	Stellenbosch Electrical Machines Finite Element Method
SANAE	South African National Antarctic Expedition
SG	Synchronous generator
S-PMC	Slip permanent magnet coupling
S-PMG	Slip permanent magnet generator
SSC	Solid state converter
SS-PMG	Slip synchronous permanent magnet generator
TS	Torque sensor
TSR	Tip-speed-ratio

Chapter 1

Introduction

The past few decades have seen a dramatic rise in the prominence of renewable energy as an alternative means of generating power. One such energy source is wind power, where electricity is most often generated using a wind turbine connected to a synchronous or induction generator.

1.1 Overview of Existing Wind Generator Topologies

Various wind generator drive train topologies exist. These topologies usually consist of at least a synchronous or induction generator, power electronics in various forms of complexity and often a gearbox. All these topologies have a set of turbine blades which transfers some proportion of the wind's kinetic energy into rotating mechanical energy. Several conventional drive train topologies are depicted in Fig. 1.1, as well as some less conventional topologies.

A very commonly used drive train is that of a gearbox connected to an induction generator, which is then connected to the grid via some form of power electronics. Fig. 1.1a shows a gearbox, induction generator and, in this case, a fully rated solid state converter (SSC), but the SSC can be replaced with various different types of power electronics, as is discussed in great detail in [1]. Another alternative layout for an induction machine is that of the doubly fed induction generator (DFIG), depicted in Fig. 1.1b, which has a wound rotor connected to a partially rated SSC, and with the stator directly grid-connected. Another variation is the use of a low speed, direct drive permanent magnet

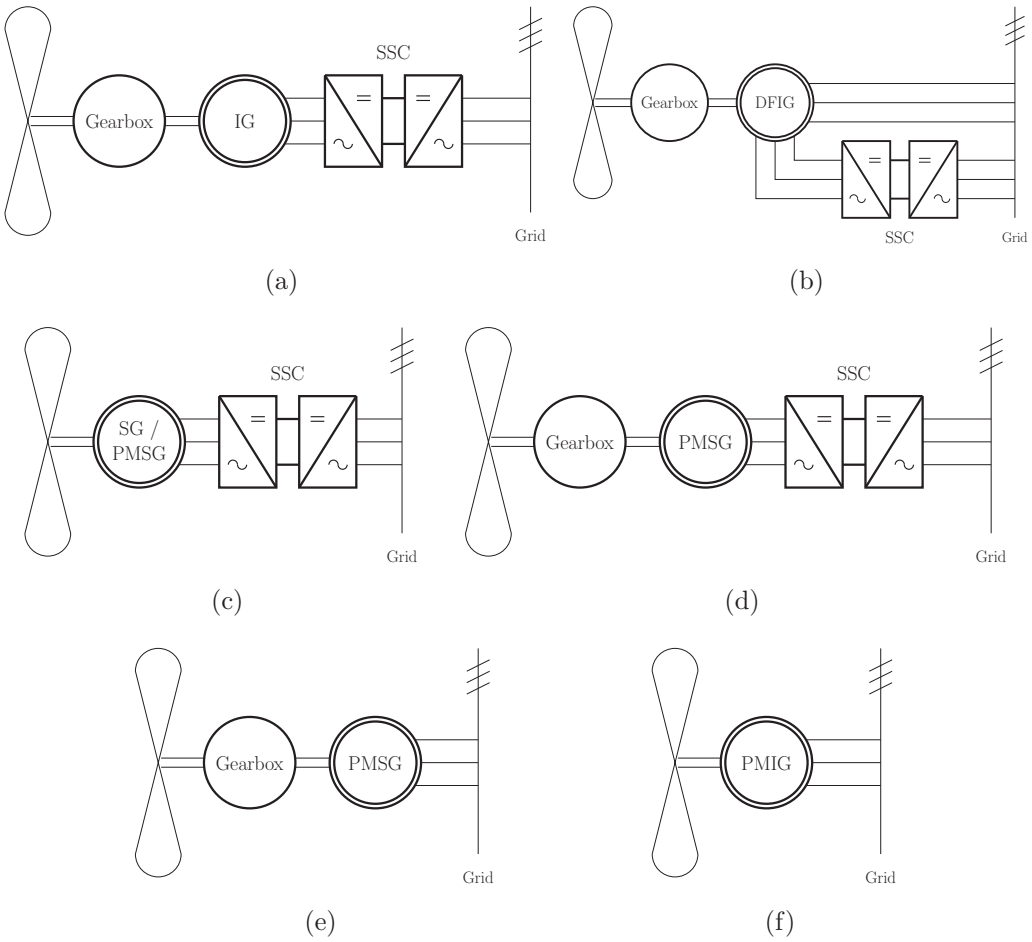

Figure 1.1: Various wind generator drive train topologies, with (a) geared IG with fully rated SSC, (b) geared DFIG with partially rated, rotor connected SSC, (c) direct drive, low speed SG with fully rated SSC, (d) geared, higher speed PMSG with fully rated SSC, (e) geared, damped, direct grid-connected PMSG and (f) direct drive, direct grid-connected PMIG.

synchronous generator (PMSG) or wound synchronous generator connected to the grid via a fully rated SSC, as depicted in Fig. 1.1c. A gearbox can be added to this set-up, as depicted in Fig. 1.1d, to allow higher operating speeds. Synchronous generators connected to wind turbines are not particularly suited to be directly grid-connected, since the transient torque introduced by wind gusts causes oscillations in the machine, which negatively affects voltage quality. This is due to the lack of damping present in an SG, unlike induction machines which have slip, which allows for a measure of damping. Attempts have been made to introduce some form of damping to SG drive trains, such as in [2] where a spring and mechanical damper is used, or in [3] where a

partially rated converter is connected to the machine's star point, or in [4] where a continuously variable transmission is used. All of these methods allow, or attempt to allow, for direct grid connection of the SG, similar to that of the drive train depicted in Fig. 1.1e. Another topology which would allow direct grid connection is that of a permanent magnet induction generator (PMIG), such as the machine investigated in [5], which is depicted in Fig. 1.1f. This is a direct drive, direct grid-connected machine, which shows great promise since no gearbox or power electronics are present, thereby providing the potential for much better reliability when compared to the other drive trains mentioned here.

1.2 Slip-Synchronous Permanent Magnet Generator Concept

A new concept PMIG was introduced and thoroughly investigated in [6], [7] and [8], which is a novel variation of the conventional PMIG. This concept is called a slip-synchronous permanent magnet generator (SS-PMG), and consists of an induction generator and a synchronous generator which share a common permanent magnet rotor, thus the two machines are mechanically connected via this common rotor. The synchronous generator (which is a PMSG) operates as per normal, with the generator running synchronously with the grid at a frequency of 50 Hz. In the concept introduced in [6] the PMSG is directly connected to the grid, without using any additional power electronic converter system. The induction generator (which is referred to in [7] as a slip permanent magnet generator, or S-PMG) does not generate any electrical power and only transfers mechanical power. The S-PMG operates in a fashion similar to that of a conventional induction generator in that the rotor windings are short-circuited, and runs at slip speed with regard to the common PM rotor which also acts as the stator for the S-PMG. The common PM rotor transfers the mechanical power of the S-PMG to the PMSG to generate electrical power.

The wind turbine blades are directly connected to the rotor of the S-PMG. The rotor of the S-PMG is magnetically connected to the PM rotor, which in turn is magnetically connected to the PMSG stator. There is no direct connection between the turbine blades and the PMSG rotor, and accordingly

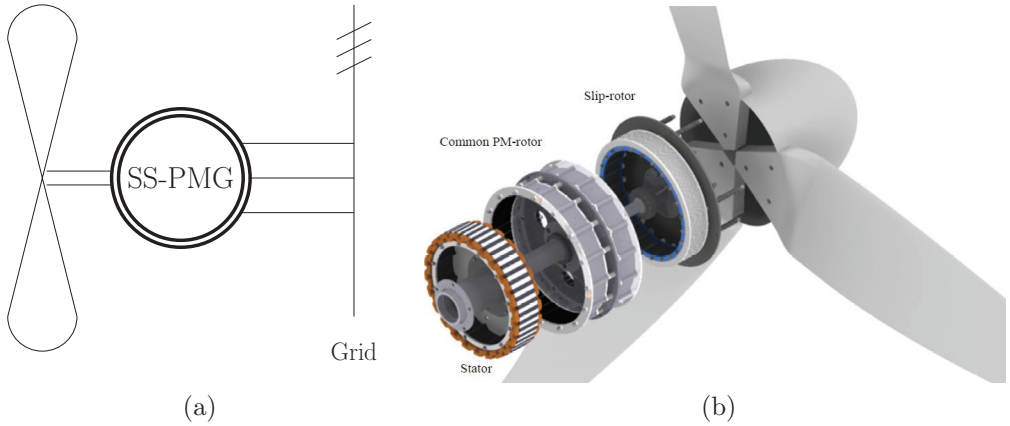

(a) (b)

Figure 1.2: (a) Diagram representing direct drive, direct grid-connected SS-PMG, as well as a (b) CAD representation [7].

the effects of sudden changes in wind speed (gusts) on generated voltages are reduced.

1.2.1 SS-PMG Drive Train

The SS-PMG drive train does not contain a gearbox, and the turbine blades are directly connected to the S-PMG, as mentioned above and shown in Fig. 1.2b. Consequently the system operates at low turbine speeds, in the case of [7] at 150 r/min. This type of system is called a direct drive system, and because of the low operating speeds the generator needs to have a high number of poles to achieve grid frequency. The large number of poles results in a complex machine design, as well as a relatively large machine. In the case of [7, 8] the SS-PMG has quite a large diameter to accommodate the large number of poles, but a proportionally short stack length.

1.2.2 Modelling and Simulation of the SS-PMG

The modelling of the SS-PMG, as described in [7], was done using dq-equivalent circuits, as is appropriate for most electric machines. Since the SS-PMG consists of two separate machines, connected via a common PM rotor, the SS-PMG was modelled using two separate sets of dq-equivalent circuits, one set for the PMSG, and one set for the S-PMG.

Finite element (FE) analysis and simulation are used along with these dq-equivalent circuits in [7] and [8] for analysis and optimisation of the SS-PMG.

During previous work on the SS-PMG, static FE simulations were used to evaluate the performance of the PMSG and S-PMG, which is much faster than using transient FE simulations. One problem with this method is that the position of the currents in both the S-PMG and PMSG are unknown. This issue is overcome by using an iterative method to determine the d- and q-axis inductances. This method is described in some detail in [6] and [7], and proves to be quite effective by converging on an operating point within three to four iterations.

It must be noted that this iterative method may not be correct in all cases, since the method relies heavily on first calculating an accurate starting value for current, for use as input for the first iteration. If this input current is not of a similar magnitude as the eventual steady-state current, then some of the metrics calculated in [6] and [7] are incorrect, specifically the flux linkage contribution made by the permanent magnets.

A further possible problem which was found with the SS-PMG modelling and simulation done in [9] is the simplification of assuming that adjacent electrically isolated coils in a multiphase S-PMG are in phase, and therefore interpreting the machine as a three phase machine. This assumption is not necessarily always accurate, but this is discussed in greater detail in Chapter 4.

1.2.3 The S-PMG as Magnetic Coupling

The S-PMG of the SS-PMG can be seen as an electromagnetic coupling, when considered on its own. This machine transfers torque magnetically and acts as a filter for torque transients. Thus the S-PMG can also be referred to as a slip permanent magnet coupling (S-PMC). The S-PMC is of particular interest in this investigation, since it is proposed that the SS-PMG be split into two separate machines, one being a conventional PMSG, and the other being a free standing S-PMC, as discussed in the next section.

1.3 Separation of the SS-PMG

In this thesis it is proposed that the SS-PMG be split into two separate machines - a PMSG and an S-PMC. The generator section can be a conventional PMSG, which is well known in literature, and widely used in industry. A free standing

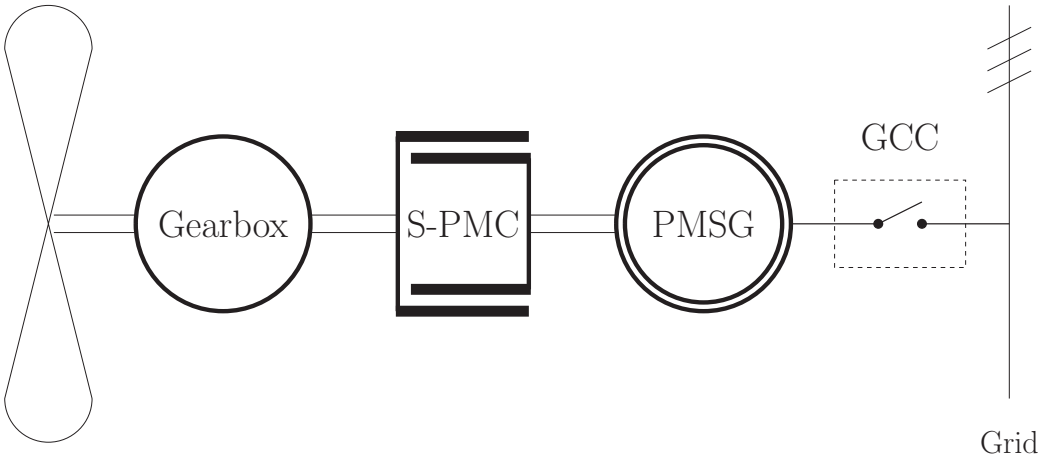

Figure 1.3: Proposed drive train topology, with gearbox, S-PMC and grid-connected PMSG

S-PMC is a relatively unknown machine, and therefore the focus in this thesis is on this machine. Fig. 1.3 depicts this concept. A gearbox is also introduced, which allows for much greater flexibility in terms of speed selection, as well as a grid connection controller (GCC), which is an electronic switch that connects the PMSG to the grid.

The S-PMC concept is investigated in depth in [9]. The S-PMC was shown to effectively maintain system stability, even for sudden, large changes in input torque, such as gusts. However, the various S-PMC's evaluated in [9] were all tested as part of an SS-PMG, and not as a free standing machine. Thus building and testing a free standing S-PMC is of great interest from a proof-of-concept point of view.

1.4 Magnetic Couplings

Eddy current and permanent magnet couplings have been around for years and have been used widely in industry. Much research [10–12] has been done on these types of couplings, and they have been characterised quite well. Magnetic couplings are primarily used in industry to increase the reliability of motors, where these motors drive a very wide range of industrial applications, including, but not limited to, conveyor belts, fans and pumps. The increased motor reliability translates into less required maintenance or motor failure, thus less downtime and lower cost. The magnetic couplings reduce and filter out

unwanted vibrations from the machinery and also prevent thermal damage due to stalling [10, 12].

A free standing S-PMC, as is proposed in this thesis, is also a coupling which transfers torque magnetically, very similar to eddy current and permanent magnet couplings. Additionally, the S-PMC operates under slip conditions, like an induction machine, where this slip is proportional to the amount of torque being transferred. The free standing S-PMC investigated in this thesis, operating under slip and being an electromagnetic coupling, is thus referred to as a slip coupler and is the main unknown in this investigation.

1.5 Problem Statement

The direct drive SS-PMG was shown to be a very promising concept, but is limited in terms of speed selection, forcing a low operating speed, which in effect also forces the machine to be quite large and bulky. The construction of the SS-PMG is also relatively complex, with two machines sharing a common PM rotor, as well as a common hub. These limiting factors warrant an investigation into an alternative drive train configuration for the same concept.

1.6 Research Objectives

In this study an alternative SS-PMG drive train layout is investigated, as depicted in Fig. 1.3, with the SS-PMG split into two halves: the slip coupler and the PMSG. Each individual component of the drive train is considered during this study. The following research objectives are investigated in this thesis:

- Wind data from the proposed wind site is used along with power coefficient curves of the chosen turbine blades to determine the potential energy yield of the drive train, and more importantly, the required input operating speed of the drive train.

- Gearboxes for large scale wind turbines are well known, however the small scale prototyping done in this investigation requires a normal, small, reduction (or down speed) gearbox to be operated in the reverse direction, thereby making it an up speed gearbox. The efficiency of the gearbox

over its load range is unknown, and this must be determined to allow calculation of the complete drive train efficiency.

- The slip coupler is the main focus of this study. A slip coupler prototype is designed, built and laboratory tested to demonstrate the feasibility of a free standing S-PMC.
- PMSGs are well known in industry, and thus a PMSG prototype is not built. However, to allow for a fair comparison of the proposed drive train with other drive trains, a PMSG prototype is designed which has the same torque and power rating as the rest of the drive train. The FE simulated torque and efficiency data are used to evaluate the efficiency of the entire drive train.
- The drive train as a whole is evaluated in terms of efficiency to determine whether it is a viable alternative to conventional power electronics controlled PMSG drive trains.

1.7 Scope of Research

The following are included in the scope of this study:

- Wind site data analysis to determine energy yield and operating speed.
- Experimental determination of gearbox efficiency.
- Finite element (FE) design of a slip coupler prototype.
- FE design optimisation of the slip coupler prototype.
- Verification of the design optimised slip coupler FE prototype using an alternative FE package.
- Use of computer aided design (CAD) to design a slip coupler prototype.
- Construction and lab testing of the slip coupler prototype.
- FE design of a PMSG prototype.
- FE design optimisation of the PMSG prototype.
- Verification of the design optimised PMSG FE prototype using an alternative FE package.

The following are out of the scope of this study:

- Construction and lab testing of the PMSG prototype.
- Grid code considerations when designing the PMSG.
- Lab testing of the entire proposed drive train.
- Field testing of proposed drive train and/or slip coupler.

1.8 Layout of Thesis

In the layout of the thesis the same order is followed as with the components of Fig. 1.3, as viewed from left to right:

- In Chapter 2 the statistical analysis of the proposed wind site data in combination with the turbine blade characteristics is investigated to determine drive train operating speed.
- In Chapter 3 the gearbox is investigated, with a specific focus on the test procedure to measure gearbox efficiency.
- In Chapter 4 the design and construction of the slip coupler prototype is detailed.
- In Chapter 5 the design of the PMSG prototype is detailed.
- In Chapter 6 the most salient results of both the measured lab tests and the simulated results are given.

Chapter 2

Wind Power Characteristics

2.1 Background

An important consideration when designing a wind turbine system is the wind energy available at the chosen wind site. This ultimately determines the amount of kWh that will be generated at the site. Thus an analysis of the wind site, using simple statistics, is of importance and is of even greater importance when selecting an operating speed for a fixed speed system, as is the case here.

2.2 Fitting of Wind Site Data to Statistical Distribution

The most common method to represent the wind speed distribution of a particular wind site is by using a Weibull distribution. To be able to fit the wind speed data associated to a particular site onto a Weibull distribution, a Weibull shape and scale parameter must be derived from the data. This can be done using several methods: the graphical method, maximum likelihood method, modified maximum likelihood method, moment method or the power density method. These methods are described and evaluated in [13] and [14]. In this investigation the maximum likelihood method is used to determine the shape and scale parameters. The method is applied to wind speed data which was recorded at the Mariendahl wind turbine testing facility outside Stellenbosch, which is the chosen wind site for this investigation. The data was recorded over a period of one year, which is seen as an adequate sample period

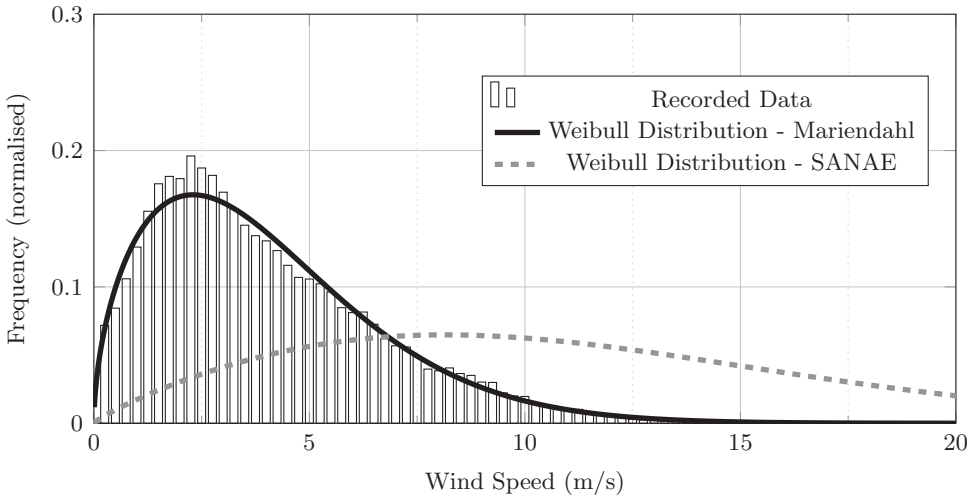

Figure 2.1: The recorded, normalised wind speed frequency plot of the Mariendahl wind site, as well as the derived Weibull distribution with $k = 1.5541$ and $\lambda = 4.4689$. The Weibull distribution for the SANAE research base is also shown, with $k = 1.839$ and $\lambda = 12.4902$.

for curve fitting purposes. The data was recorded in ten minute averages over this period. The probability density function $f(v)$ of a Weibull distribution is given by

$$f(v) = \frac{k}{\lambda}\left(\frac{v}{\lambda}\right)^{k-1} e^{-\left(\frac{v}{\lambda}\right)^k} \tag{2.1}$$

with k as the shape parameter, λ as the scale parameter and v as the wind speed. The shape and scale parameters for Mariendahl were calculated to be $k = 1.5541$ and $\lambda = 4.4689$. The Weibull distribution for the chosen site at Mariendahl is shown in Fig. 2.1. The originally recorded data points are also plotted using bars, to illustrate the relative accuracy of the Weibull fitting. Additionally, the Weibull distribution for a second site is included for comparison purposes. The Weibull distribution for the wind site at the SANAE (South African National Antarctic Expedition) base, with $k = 1.839$ and $\lambda = 12.4902$, is also given in Fig. 2.1. The SANAE wind site is known to have a very high average wind speed, and is thus a very good wind site.

The Weibull distribution is one of two very important pieces of information required to evaluate wind turbine performance, the second being the turbine blade wind power coefficient (C_p) vs Tip-speed-ratio (TSR) curve, as dealt with in the next section.

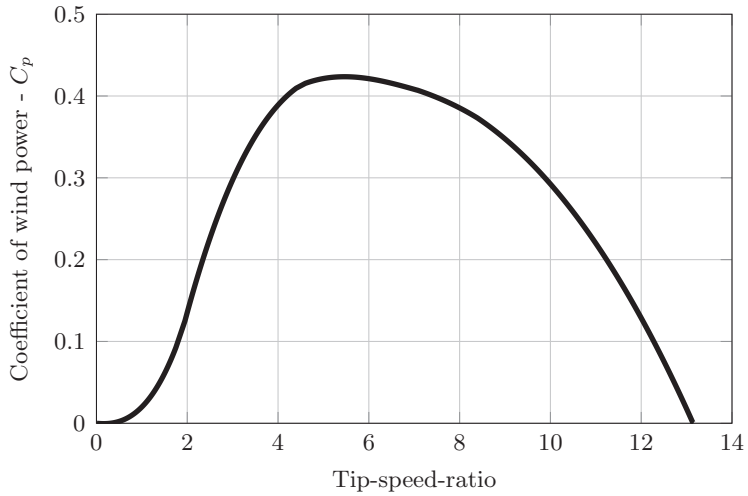

Figure 2.2: Coefficient of wind power versus tip-speed-ratio curve.

2.3 C_p vs Tip-Speed-Ratio Curve

Any wind turbine blade set can be characterised by a C_p vs Tip-speed-ratio (TSR) curve. The coefficient of wind power (or C_p) value is a fraction indicating the amount of power extracted by the turbine blades from the total power available in the wind. The TSR is defined as

$$\text{TSR} = \frac{\omega R}{v} \tag{2.2}$$

where ω is the angular turbine rotor speed (in rad/s), R the radius of the rotor swept area (i.e. length of a single blade) and v once again the wind speed. The C_p vs TSR curve (as provided by the manufacturer) for the blades used in this investigation is shown in Fig. 2.2, with $R = 1.9$ m.

2.4 Power Available in the Wind

The power available in the wind (in Watts) is defined as the amount of kinetic energy (in Joules) passing through a given area over time [15]. The kinetic energy can be calculated using (2.3), where m is the mass of air being evaluated. The mass flow rate of air is $\rho A v$, with ρ being the density of air (1.225 kg/m^3 reference value, 1.18kg/m^3 for Stellenbosch), and A the swept area of a wind turbine. Combining this with (2.3), we obtain (2.4), which is used to calculate the available power in the wind (P_w).

$$\text{Kinetic Energy} = \frac{1}{2}mv^2 \tag{2.3}$$

$$P_w = \frac{1}{2}\rho A v^3 \tag{2.4}$$

The coefficient of wind power (C_p) indicates the actual fraction of power that is extracted from (2.4) by the wind turbine. Thus, similarly to the method followed by [15, 16], we can write

$$P_m = \frac{1}{2}\rho C_p A v^3 \text{ or } P_m = \frac{1}{2}\rho\pi C_p R^2 v^3 \tag{2.5}$$

with P_m denoting the mechanical power extracted from the wind by the turbine blades. Combining (2.2) with (2.5) allows us to write P_m in terms of the C_p, TSR and turbine speed:

$$P_m = \frac{1}{2}\rho C_p A \left(\frac{\omega R}{\text{TSR}}\right)^3. \tag{2.6}$$

Equation (2.6) is very useful in that it allows us to plot the expected mechanical turbine power against the turbine rotational speed, for various wind speeds. The TSR is calculated using (2.2), for a given wind speed and turbine speed, and the corresponding C_p value is attained from Fig. 2.2. These values are then used along with (2.6) to plot turbine power against turbine speed.

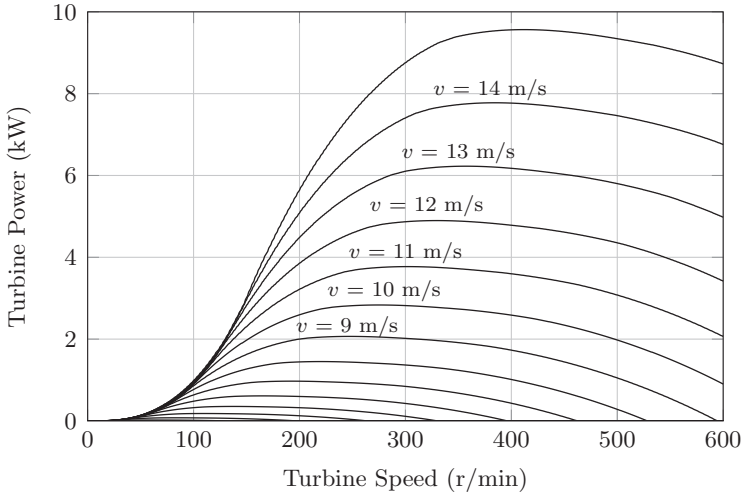

Figure 2.3: Turbine power versus turbine speed for $v = 1$ to 15 m/s.

The result is given in Fig. 2.3, and we can use this to estimate the kW rating and/or operating speed of a generator (as well as the slip coupler, in the case of this investigation), as is illustrated in the following section.

2.5 Selection of Generator Size

The selection of generator size is an important consideration in any machine design process. In the case of this investigation the wind turbine is fixed pitch and is required to use stall-control (where no pitch control is used and the blades are designed to have a reduced efficiency at higher wind speeds [15]). The turbine is also fixed speed, thus Fig. 2.3 can be used to visually determine a suitable generator kW rating. For this fixed speed, stall controlled system the desired operating speed range is more or less where the instantaneous turbine power strives towards saturation, which is usually at high (> 10 m/s) wind speeds. This is where the high wind speed plot lines in Fig. 2.3 are tightly spaced, in this case for a turbine speed between 0 and 180 r/min. This area is shown in Fig. 2.4. Since it is required that the turbine be stall-controlled, the rated generator size should fall somewhere in this area, thus between 0 and 4 kW.

In this investigation a prototype of the slip coupler is built, and it is decided that the real power output of the slip coupler should roughly conform to standard motor power ratings, thus 1.5, 2.2, 3.0 or 3.7 kW (at least 1.5 kW minimum rating). Factoring in the desired slip coupler efficiency of 97% and the estimated gearbox efficiency of 98%, and assuming operation at rated power, the possible ratings as viewed from the turbine side, are 1.57, 2.31, 3.16 and 3.89 kW.

For any fixed turbine speed the power output over the range of feasible wind speeds can be taken and multiplied with the Weibull probability density function (frequency versus wind speed, which is normalised over a year period i.e., multiplied with 8760 hours) to obtain a plot of the annual energy produced versus wind speed. The area under this curve, for a given turbine speed, is equal to the total annual energy produced for that fixed turbine speed.

If the total annual energy production for various fixed turbine speed values are calculated, then the energy yield for the different speeds can be compared and an optimal (or near optimal) operating speed can be selected. In this

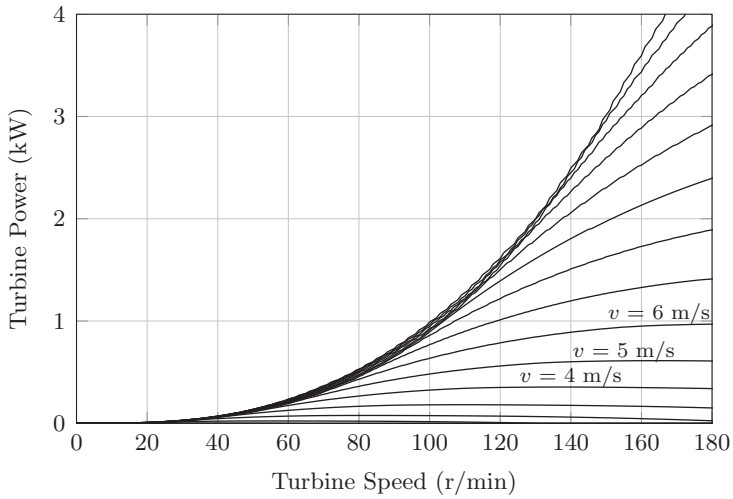

Figure 2.4: Turbine power versus turbine speed over the range of 0 to 180 r/min, once again for $v = 1$ to 15 m/s.

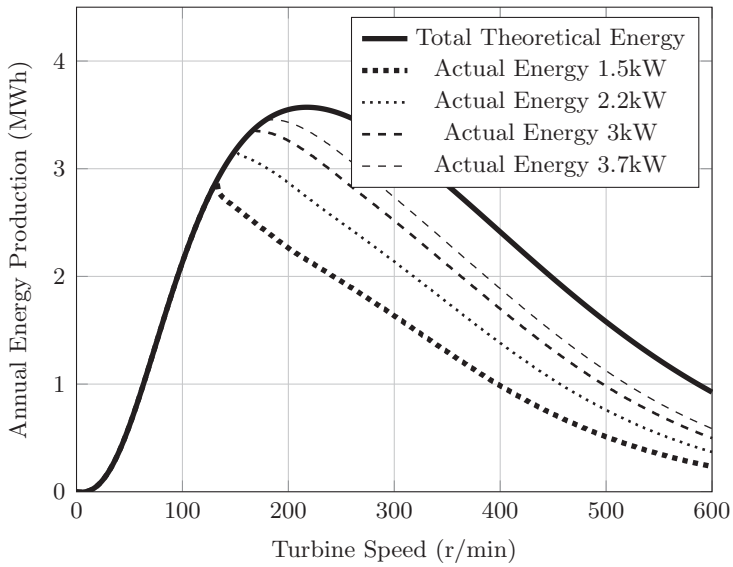

Figure 2.5: Annual energy versus turbine speed for the Mariendahl wind site.

case, optimal turbine operating speed refers to the speed which would generate the most energy, in kWh, per year. To this end a plot of fixed turbine speed (for the range 0 to 600 r/min) versus annual energy production is generated, and given in Fig. 2.5 for Mariendahl, and Fig. 2.6 for SANAE. This allows us to quickly identify the operating speed range in which near optimal energy yield can be achieved. Note that the actual energy yield for the power ratings being evaluated is less than the theoretical energy. This is due to a machine

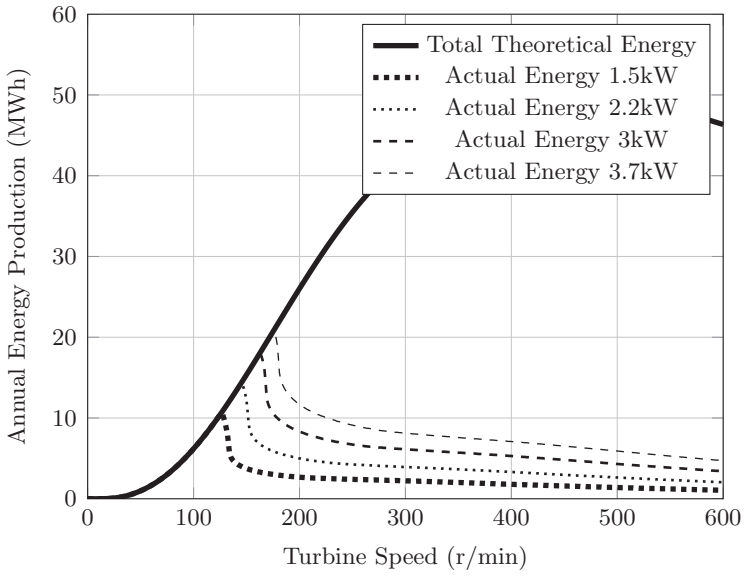

Figure 2.6: Annual energy versus turbine speed for the SANAE wind site.

service factor, chosen as 1.35, imposed on the PMSG. The machine is allowed to operate at only 1.35 times its rated power, and thereafter is shut down to protect the machine, meaning that any energy produced by winds containing more than 1.35 times the rated power will not be harvested.

The annual energy production in Fig. 2.5 and Fig. 2.6 is also used to calculate the capacity factor versus turbine speed for the various power ratings. This is done by dividing the annual energy by the maximum theoretical annual energy production (rated power x 8760 hours per year). The results are given in Fig. 2.7 and Fig. 2.8.

The main results given in Fig. 2.5 and Fig. 2.7 are summarised in Table 2.1. Similarly the results in Fig. 2.6 and Fig. 2.8 are summarised in Table 2.2. Some interesting observations can be made from this data. Firstly, looking only at the Mariendahl results, the annual energy yield of the 3.7 kW system is only marginally better than the 3 kW system, thus the 3.7 kW system will not even be considered. The remaining three options all have certain merits which would make them good choices, be it a high capacity factor, high energy yield or a good mix between the two. In comparison, the results for the SANAE wind site in Table 2.2 are very different. The annual energy yield is considerably higher, for all four machine ratings, consistent with a better wind site. Fig. 2.6 also indicates that not one of the four machines come close to reaching the maximum

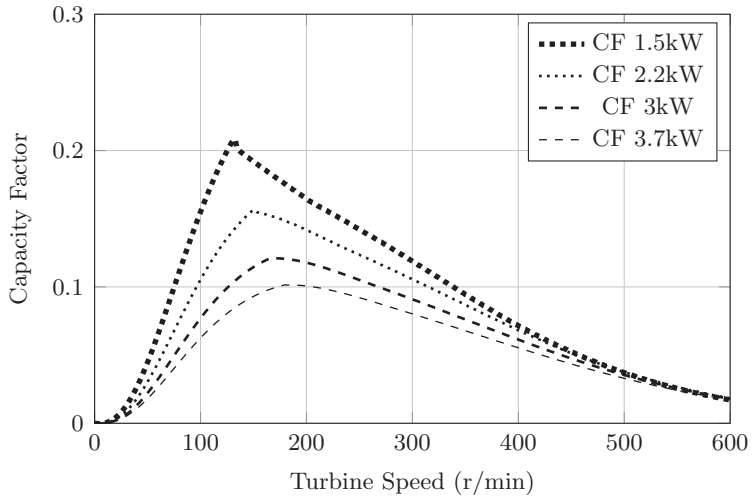

Figure 2.7: Capacity factor versus turbine speed for the Mariendahl wind site.

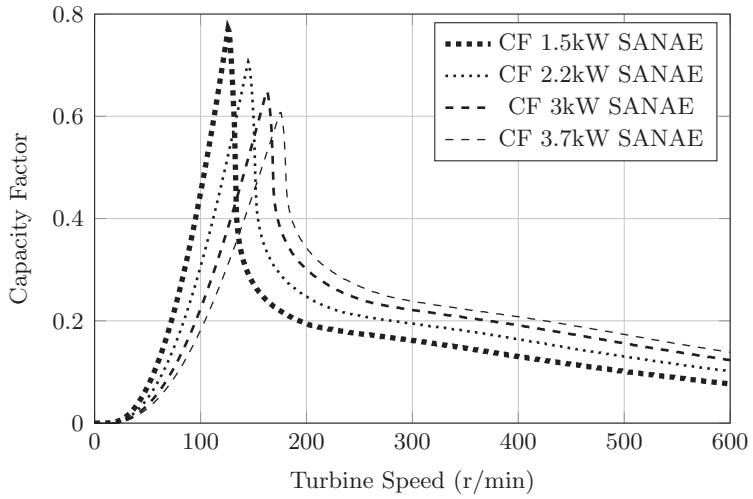

Figure 2.8: Capacity factor versus turbine speed for the SANAE wind site.

theoretical energy available at the site, thus the four machine ratings are far too small to extract the full potential of the energy that could be harvested by the turbine blades. Although a lot more energy is potentially available at the SANAE wind site, the smaller ratings do result in a very good capacity factor (almost 0.8 for the 1.5 kW). Ultimately the best choice of machine rating will very much depend on the fixed cost associated with setting up the entire system, and will almost certainly favour the larger power ratings. For this investigation (which focuses only on the Mariendahl data) it was decided that the safe middle ground would be chosen, and as such a selection was made

based on a good mix between capacity factor and energy yield - thus 2.2 kW was chosen as the rated power for the slip coupler which is designed and built in this investigation.

Table 2.1: Annual power generation and capacity factor for various slip coupler/generator ratings (Mariendahl)

Rating [kW]	Turbine Power [kW]	Annual Energy [kWh]	CF	Turbine Speed [RPM]
1.5	1.57	2865	0.208	132
2.2	2.31	3167	0.157	151
3	3.16	3362	0.121	168
3.7	3.89	3454	0.101	185

Table 2.2: Annual power generation and capacity factor for various slip coupler/generator ratings (SANAE)

Rating [kW]	Turbine Power [kW]	Annual Energy [kWh]	CF	Turbine Speed [RPM]
1.5	1.57	10 596	0.77	126
2.2	2.31	14 300	0.707	145
3	3.16	17 967	0.649	163
3.7	3.89	20 696	0.607	176

2.6 Selection of Generator Speed

In Table 2.1 it is shown that the optimal turbine operating speed for a 2.2 kW rated system is 151 r/min. In reality this exact speed can very seldom be used due to system constraints, such as available gearbox ratios (if a gearbox is used) and generator pole number, which determines the generator's synchronous speed.

In this investigation the drive train consists of the turbine blades, a gearbox, the slip coupler and finally the grid-connected generator. The generator is chosen to operate in the medium speed range (between 150 and 750 r/min). Thus for a grid frequency of 50 Hz the available pole numbers are from 8 to 40. The generator chosen for this investigation is a 10-pole machine, thus the synchronous speed on the high speed side is 600 r/min. The slip coupler is connected to the input side of the generator, thus the output speed of the slip

coupler is also 600 r/min. With a rated slip of 0.03, the slip coupler input speed is $600 \div 0.97 = 618.55$ r/min. Now we require a gearbox with a ratio of roughly $618.55 \div 151 = 4.1$. The closest gearbox ratio available for this investigation was 1:3.78, thus the turbine blades are forced to operate at $618.55 \div 3.78 = 163.64$ r/min. This gives an annual energy yield of 3092 kWh, and a capacity factor of 0.153.

It could be argued that under these circumstances, where several speed constraints are present, it is worthwhile to select a different power rating, such as a 3 kW, since the energy yield will be 3323 kWh, and the capacity factor 0.12, but this does not appear to be a very significant gain in capacity. Conversely, the 1.5 kW under these conditions would generate 2539 kWh per year, with a capacity factor of 0.185. This selection will be very dependent on the annual cost per kWh of a given system - the variable cost associated with building the actual slip coupler and/or generator, the maintenance, as well as the fixed cost for the gearbox, turbine blades, grid controller, tower etc. The costing aspect is not within the scope of this investigation, and thus the chosen 2.2 kW power rating will remain, but this method does provide an analyst with the ability to compare different machine sizes, as well as to identify the preferred operating range of speeds for a given machine.

2.7 Concluding Remarks

In this section it is found that the desired power rating of the slip coupler is around 2.2 kW, and assuming a high generator efficiency, the rated output power of the PMSG is chosen to also be 2.2 kW. The desired synchronous speed of the PMSG is found to be 600 r/min, which implies an input speed of 618.55 r/min for the slip coupler, at rated conditions. These parameters are used to design the drive train, slip coupler and PMSG.

Chapter 3

Characterising the Mechanical Gearbox

The gearbox is one of the major components in the drive train being investigated in this project. To be able to assess overall system efficiency, it is very important that the efficiency of the gearbox be known, since accurate data cannot be provided by the manufacturers. In this project an up-speed gearbox is required to increase the drive train rotational speed from 163 r/min to 618 r/min, which is an increase of roughly four times. Up-speed gearboxes for low power ratings are not readily available for industrial applications, and almost all commercial models are down-speed (reduction) gearboxes. Thus in this investigation a reduction gearbox is run in the reverse direction, thereby making it an up-speed gearbox. The direction reversal creates uncertainty with regard to the efficiency and reliability of the gearbox.

3.1 Gearbox Details

In this project an *SEW Eurodrive* gearbox is used, with a gear ratio of 1:3.78, maximum torque of 305 Nm (well above the rated low speed torque of 132 Nm) and a continuous power rating of around 5 kW. The manufacturer claims an efficiency of about 97 % under normal operating conditions, however the gearbox used will be run in the reverse direction, and thus the efficiency at various torque levels is an unknown.

The gearbox is a single stage, helical gear unit, which is a simple and reliable design. A single stage gearbox also implies that the efficiency should be quite

high. Another option is to consider a planetary gearbox, which allows for a smaller form factor for the same rated torque. Higher gear ratios for the same form factor are also achievable when comparing planetary to helical gear units.

In this study simplicity and reliability are very important considerations, and thus the helical gear unit is used.

3.2 Test Set-up

The efficiency of the gearbox is experimentally determined, which in turn enables the evaluation of the entire drive train efficiency. The test set-up used to evaluate the gearbox efficiency is illustrated in Fig. 3.1, and pictures of the actual test set-up used are shown in Fig. 3.2. The set-up consists of a large 55 kW induction motor (IM) used to drive the system, torque sensors (TS) placed before and after the gearbox, and a DC machine on the opposite side which is run as a generator. The DC generator is loaded up via external resistors to increase the load applied to the gearbox. The torque and speed of both torque sensors are recorded at different load levels, allowing the input and output power to be calculated. This, in turn, allows the calculation of efficiency.

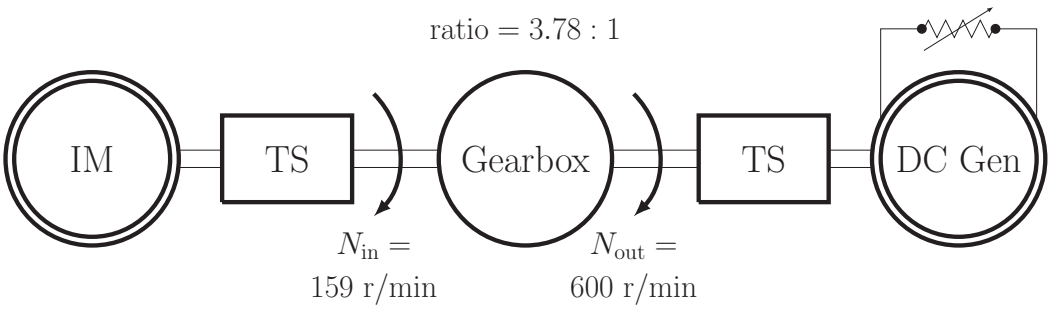

Figure 3.1: Diagram illustrating the test set-up used to test the gearbox.

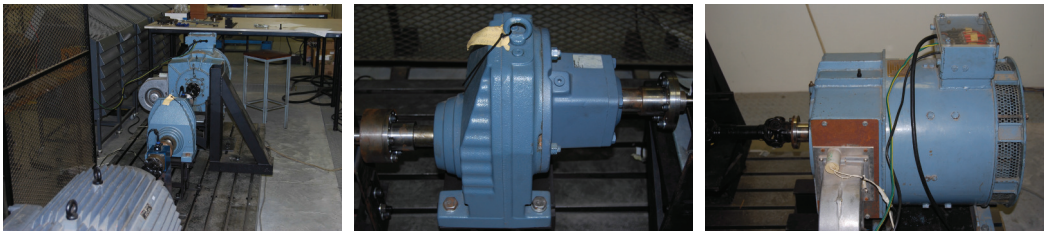

(a) (b) (c)

Figure 3.2: Gearbox test bench set-up, with (a) a view of the entire set-up, with the induction motor in the foreground. A close-up of (b) the gearbox as well as (c) the DC generator is given

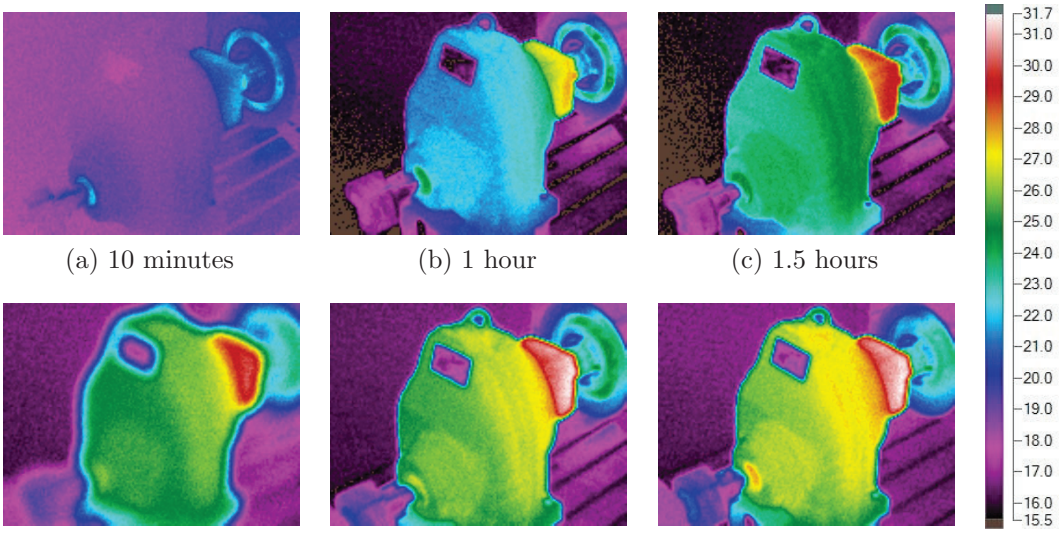

(a) 10 minutes (b) 1 hour (c) 1.5 hours

(d) 2 hours (e) 2.5 hours (f) 3 hours

Figure 3.3: Surface temperatures of the gearbox after running at load for various time periods, between 10 minutes and 3 hours. The scale, in °C, is also given.

3.3 Thermal Considerations

During early gearbox testing it is observed that the efficiency is noticeably affected by the operating temperature of the gearbox. The efficiency is much lower when the gearbox is still at room temperature, but increases as the operating temperature increases. The efficiency stabilises as the gearbox reaches a constant operating temperature. The gearbox is run at full load (35 Nm output) for approximately 1.5 hours before it reaches this constant operating temperature. Fig. 3.3 indicates the surface temperatures of the gearbox after running at full load for various time periods.

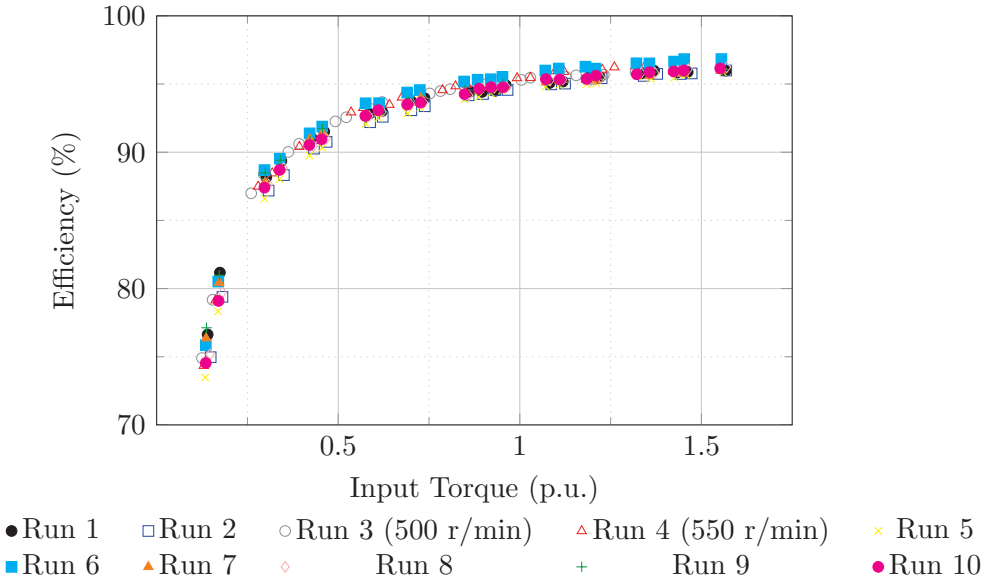

Figure 3.4: Experimental results of ten independent gearbox tests of efficiency versus input torque, with the majority conducted at 600 r/min (rated torque = 132 Nm).

The gearbox is initially at room temperature, and warms up considerably after an hour of running at full load. Subsequent heating seems to be less pronounced after the first hour, with the surface temperature only rising about 2 to 3 °C between hours one and two. Between 1.5 hours and 3 hours there is a temperature rise of only 2 °C. Thus it is assumed that the gearbox reaches thermal equilibrium after running at full load for more or less 1.5 hours. This assumption is also supported by efficiency measurements made throughout testing.

3.4 Results of Performance Tests

The gearbox is initially tested at an output speed of 600 r/min, which is very close to the rated input speed of the slip coupler (618 r/min). The gearbox is tested throughout a load range of no load to about 1.5 p.u. (52 Nm on the high speed side, 200 Nm on the low speed side). The tests are repeated several times, and on different days, to ensure that the results are consistent and repeatable. The data of ten independent gearbox tests are given in Fig. 3.4, with the data following a clear trend. The efficiency is relatively low (below 80%) at loads below 0.25 p.u., but rapidly increases up to 96% at rated loads of 132 Nm (1

p.u.). Note that the figure is given as a function of input torque, hence rated torque is $35 \times 3.78 = 132$ Nm.

Two of the runs were conducted at output speeds other than 600 r/min, specifically 500 and 550 r/min. Note that runs conducted at speeds above 600 r/min, such as 650 and 700 r/min, were not included since the DC generator exhibited unwanted vibrations at these speeds. The runs at 500 and 550 r/min are used to illustrate that the efficiency versus input torque remains unchanged despite the change in speed, meaning that this characteristic is speed independent for minor variations in speed. This is especially useful for our analysis, since the input speed of the slip coupler varies depending on slip, and thus the output speed of the gearbox will also vary with load when considering the drive train as a whole.

3.5 Concluding Remarks

The efficiency of the gearbox is found to be around 96-97% at a rated load of 132 Nm. It is very important to note that this efficiency can only be achieved if the gearbox is brought to operating temperature by running the gearbox at full load for at least 1.5 hours before testing. This warm-up period must also be applied to any subsequent tests where the gearbox is included, to ensure accurate results.

Chapter 4

Design of Slip Coupler

The slip coupler, as highlighted in Fig. 4.1, is one of the main unknowns in the proposed drive train, and is thus one of the main focuses of this thesis. The slip coupler is potentially a very interesting and relevant machine to investigate, and therefore the focus in this chapter is on the complete design and optimisation of a slip coupler prototype, with the intention of building the prototype. The slip coupler operating parameters are determined in Chapter 2, with the operating speeds being 618.6 r/min (input), 600 r/min (output) with a desired efficiency of 97% and 35 Nm torque at a rated slip of 3%. Some problems are encountered regarding the analysis of the slip coupler due to its unusual design, but these problems are addressed. This chapter yields a near-optimal design of a 28 pole, 30 phase slip coupler and also details the construction of a prototype. The prototype is evaluated later in this thesis.

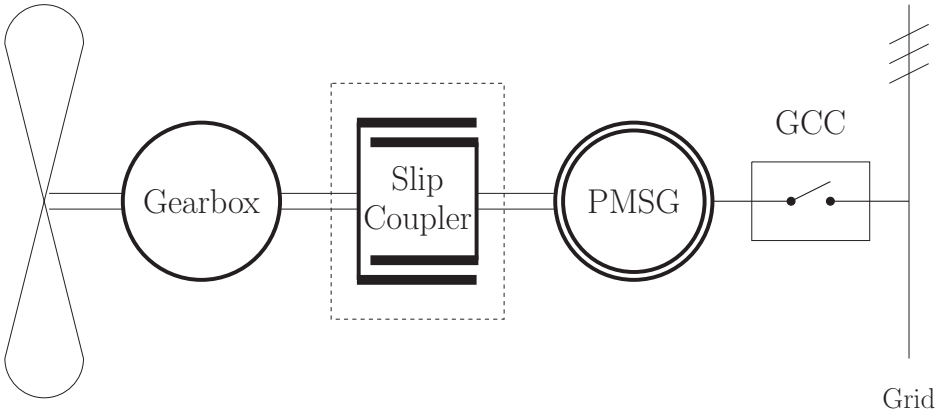

Figure 4.1: The proposed drive train topology, with the slip coupler highlighted.

4.1 "Slip Coupler" Concept

As mentioned earlier, in this thesis it is proposed that the PMSG and S-PMC sections of the SS-PMG be split into two separate machines, still on the same drive train, with a gearbox added to the drive train, as shown in Fig. 4.1. Work in [9] following from [7] introduces a S-PMC design which consists of double layer, non-overlap windings. This simplified construction is very attractive, and consists of pairs of adjacent conductors shorted at the end windings, creating a 48 phase machine (as was the case in [9]). Following from this concept, a double layer, non-overlap winding short circuited PM motor, operating under slip conditions, is investigated in this thesis, and as mentioned earlier, is referred to as a slip coupler. The slip coupler investigated and designed in this thesis is a 28 pole, 30 slot machine with double layer windings. Similar to the S-PMC detailed in [9], pairs of adjacent conductors on the same winding layer are shorted at the end windings, thereby creating a machine with 30 non-overlap, individual coils, and consequently 30 separate phases. The slip coupler design is kept as simple as possible and consists of two rotating sections: the wound rotor (the inner section, containing the windings), and the PM rotor (the outer section, lined on the inside with PMs). The coils are solid aluminium bars, with the possibility of using laminated aluminium plates in the final design, for ease of construction. The initial design is given in Fig. 4.2a, but this design is updated with larger coils in the upper winding layer, with the result shown in Fig. 4.2b. A 3D representation of this design is shown in Fig. 4.3a, as well as an individual coil in Fig. 4.3b. The second design in Fig. 4.2b is chosen for the slip coupler, due to better slot space utilisation.

The analysis and FE modelling in [9] was done with the assumption that the current magnitudes in the upper and lower coils of the S-PMC are equal, and that groups of adjacent coils, which are not electrically connected, are in phase. These assumptions allow the multiphase machine to be interpreted as a three phase machine, greatly simplifying the analysis. These assumptions are not necessarily correct, and an alternative formulation must be found to enable the analysis of such multiphase, double layer S-PMCs. It is clear from Fig. 4.2b that the coil areas differ between the upper and lower layer coils. The difference in coil area implies a different impedance value between the upper and lower layer coils, which will result in a different current magnitude between

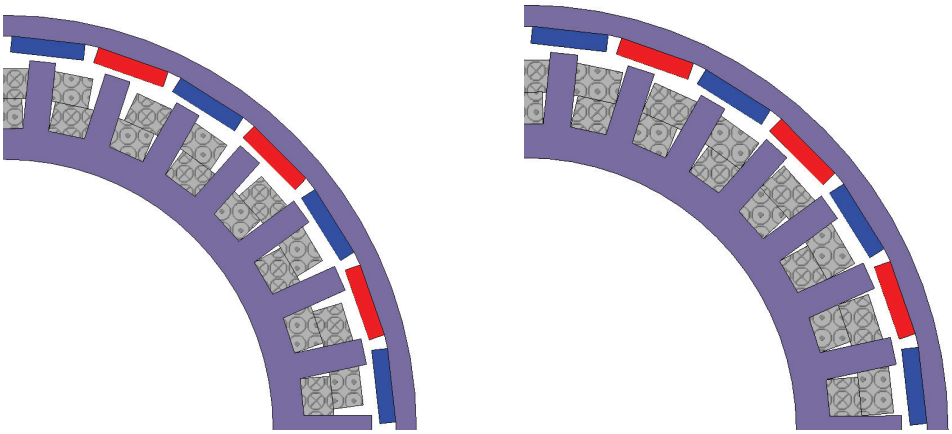

(a) (b)

Figure 4.2: (a) Initial slip coupler design, (b) updated slip coupler design (with larger upper coil). Note the use of PM's on the outer ring (or PM rotor) [17].

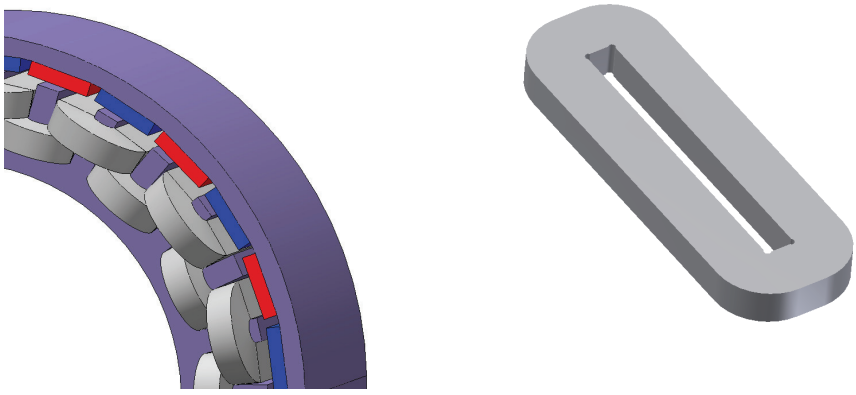

(a) (b)

Figure 4.3: (a) A 3D representation of the active components of the slip coupler [17]. Note the individually short circuited coils on the wound rotor, with each coil representing a phase. A single coil is also shown in (b).

the upper and lower layer coils.

The analysis of the slip coupler thus presents the machine designer with an interesting problem. To the knowledge of the author, no technique currently exists to enable the analysis of a 30 phase, double layer induction machine in the dq reference frame, where none of the coils are in phase, and the current magnitudes differ between the upper and lower coils. Authors of existing literature [18, 19] exploring the dq modelling of multiphase machines generally make the assumption that current magnitudes are equal across all phases, thereby allowing the expansion of the dq transformation matrix to any number of balanced phases. This traditional method does not work when the current magnitudes differ between phases (or winding layers, as is the case with the slip coupler). A novel analysis technique, initially proposed in [17], is used in this investigation to allow the analysis, dq modelling, and eventual optimisation of the slip coupler.

4.2 Proposed Analysis Technique

The waveforms of current and induced voltage in the wound rotor coils are assumed to be sinusoidal. This assumption can be made for non-overlap windings used in rotating machines. This implies that the dq transformation of phase currents should yield DC values of dq currents. The dq modelling of such a machine has not been done before (to the knowledge of the author), and can prove to be difficult. The fact that the cross sectional area differs between the upper and lower layer coils causes the current magnitudes to also differ between the upper and lower layer coils. This means that existing analysis methods are no longer valid for the slip coupler. Standard dq-transformation cannot be performed on the slip coupler, and is thus not sufficient for the analysis of the slip coupler. An alternative interpretation of the slip coupler is proposed to enable the use of dq analysis.

Following from the work done in [17], with N_{ph} phases (each shorted coil is a phase), we divide the phases into sets of three. The slip coupler has 30 phases, and thus we have 10 sets of three, or more generally we have $N_{ph}/3$ sets. In line with standard three phase analysis, we group phases together which are 120 electrical degrees apart (or some multiple of 120 degrees). Each of the $N_{ph}/3$ sets thus contains three phases which are 120 electrical degrees apart,

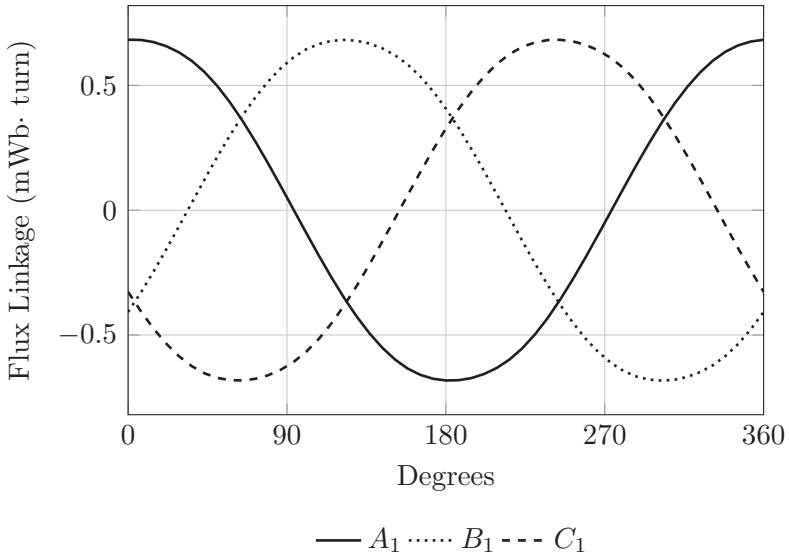

Figure 4.4: Flux linkages of phases A_1, B_1 and C_1 (as per Fig. 4.5), over 360 electrical degrees [17].

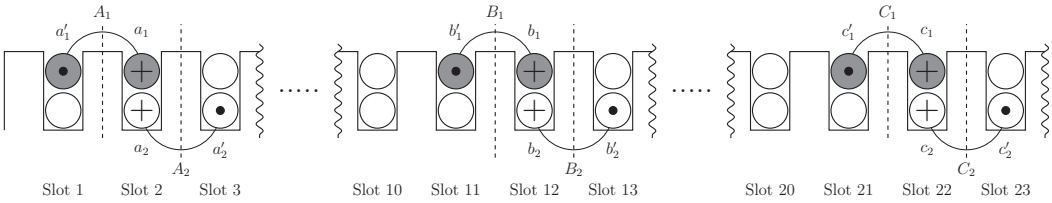

Figure 4.5: Diagram illustrating the spatial distribution of coils around the wound rotor. Each highlighted coil set is individually shorted, and thus represents a phase (e.g. coil $a_1 + a'_1$ is shorted at both ends, and is thus one phase out of the total 30 phases). For the purposes of this analysis the phases are grouped together in sets of three, and each set is interpreted as an individual three phase machine. The coils highlighted in the figure $(a_1 + a'_1, b_1 + b'_1, c_1 + c'_1)$ are spatially divided by 120 degrees, and together form one set of three phases. The phase axes for the set are given by A_1, B_1 and C_1. There are $N_{ph}/3$, or ten, sets in total on the machine [17].

effectively creating $N_{ph}/3$ balanced three phase machines. For the chosen slip coupler design of a 28/30 pole slot combination, phases which are divided by 120 electrical degrees also happen to be divided by 120 spatial degrees, however, it must be noted that this will not always be the case. In the case of the slip coupler we convert the 120 spatial/mechanical degrees to electrical degrees by multiplying by poles/2:

$$120 \times \frac{28}{2} = 1680 \text{ degrees.}$$

We now subtract 360 degrees four times:

$$1680 - (360)(4) = 240 \text{ degrees (electrical)}$$

which is also equivalent to -120 electrical degrees. Thus, when considering Fig. 4.5, the spatial angle between A_1 and B_1 is 120 degrees, and the corresponding electrical angle is 240 degrees. In exactly the same fashion it can be shown that the electrical angle between A_1 and C_1 is 120 degrees. To illustrate this concept the flux linkages of these three phases (A_1, B_1 and C_1), over a period of 360 electrical degrees, are shown in Fig. 4.4. From Fig. 4.4 it is clear that phases A_1, B_1 and C_1 together form a balanced three phase set. It is important to note that, as is the case for phases A_1, B_1 and C_1, all three phases must come from the same winding layer. If they are not from the same layer, the method will not work, since the current magnitudes in the set will not be equal.

Fig. 4.6a shows the spatial distribution of the phase axes in vector format, as they appear around the wound rotor. A_1, B_1 and C_1 from Fig. 4.5 can be illustrated as A_i, B_i and C_i in Fig. 4.6a, with $i = 1$. The subscript i denotes the set number for one set of three phases (with $i = 1, 2, ... \ N_{ph}/3$), where these three phases are grouped as described above. If this grouping process is completed, the slip coupler can be interpreted as $N_{ph}/3$ sets of balanced three phase quantities. These $N_{ph}/3$ sets are separately transformed to the dq reference frame and analysed in exactly the same way normal three phase machines are analysed. The torque value obtained from each set is summed to determine the total torque of the slip coupler.

This method is relatively simple, since each individual set can be analysed using classic three phase analysis, and all existing formulas and techniques are still valid and need not be adapted. This method is also very useful for machines such as the slip coupler, since it enables us to analyse machines where the current magnitudes are not equal in the top and bottom windings.

Another potential method to analyse the slip coupler would be to group all the top layer coils together, and similarly group all bottom layer coils. The entire group of (in this case) 15 phases in a single layer are then transformed to the dq reference frame, using a transformation matrix adapted for 15 phases. This yields two sets of dq quantities, upon which dq analysis can be done, and the torque values of the two layers summed to get the final torque value. This

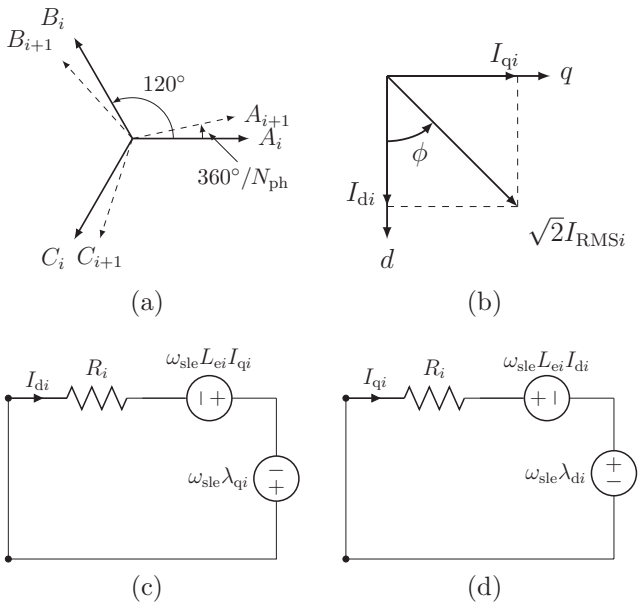

Figure 4.6: (a) Diagram illustrating the distribution of various phase axes around the rotor, where one three phase set shares a like subscript. The (b) vector diagram for the ith set of three phases are given, as well as the corresponding (c) d-axis and (d) q-axis equivalent circuits [17].

method requires modification of the dq transformation matrix, to be able to accommodate 15 phases, as well as modification of most of the existing formulas for torque and other performance metrics. This method is not overly difficult and should work equally well, but was not used in this analysis.

4.3 Slip Coupler Equivalent Model

The slip coupler generates torque in a manner similar to the way an induction machine does, the only difference is that the stator of the induction machine, which has a rotating magnetic flux field generated by the three phase coils, is replaced by a rotating ring of permanent magnets, which also results in a rotating magnetic flux field.

As mentioned earlier, for this analysis method the slip coupler is divided into 10 sets of balanced three phase quantities. Five of these sets are in the upper layer, and five sets in the lower layer, as in Fig. 4.5. For ease of reference the upper layer sets are numbered $i = 1, 3, 5, 7, 9$ and the lower layer sets $i = 2, 4, 6, 8, 10$. The RMS phase currents in the upper layer phases are

identical, and this means that the dq currents must also be the same:

$$I_{\mathrm{d1}} = I_{\mathrm{d3}} = I_{\mathrm{d5}} = I_{\mathrm{d7}} = I_{\mathrm{d9}} \tag{4.1}$$

$$I_{\mathrm{q1}} = I_{\mathrm{q3}} = I_{\mathrm{q5}} = I_{\mathrm{q7}} = I_{\mathrm{q9}}. \tag{4.2}$$

The dq currents in the lower layer phases are also the same:

$$I_{\mathrm{d2}} = I_{\mathrm{d4}} = I_{\mathrm{d6}} = I_{\mathrm{d8}} = I_{\mathrm{d10}} \tag{4.3}$$

$$I_{\mathrm{q2}} = I_{\mathrm{q4}} = I_{\mathrm{q6}} = I_{\mathrm{q8}} = I_{\mathrm{q10}}. \tag{4.4}$$

The dq currents are transformed to the phase domain using

$$\mathbf{I}_{\mathrm{abc}(i)} = \mathbf{K}_{\mathrm{p}}(\theta_i)\mathbf{I}_{\mathrm{dq}(i)} \tag{4.5}$$

with

$$\theta_i = (i-1)\delta \qquad i = 1, 2, \ldots, 10 \tag{4.6}$$

where $\delta = (360/N_{\mathrm{ph}})(p/2)$, δ is the slot-pitch angle (in electrical degrees), p the number of poles and N_{ph} the number of phases. $\mathbf{K}_{\mathrm{p}}(\theta_i)$ is Park's transformation, as a function of (θ_i), which represents the angle between the d-axis and the wound rotor phase A axis for set i. In the FE package used in this analysis, the phase currents are used as input, and then the resulting phase flux linkages $(\boldsymbol{\lambda}_{\mathrm{abc}(i)})$ are obtained as output. These flux linkages are transformed back to the dq domain using

$$\boldsymbol{\lambda}_{\mathrm{dq}(i)} = \mathbf{K}_{\mathrm{p}}^{-1}(\theta_i)\boldsymbol{\lambda}_{\mathrm{abc}(i)}. \tag{4.7}$$

The short-circuited dq-equivalent circuits are given in Fig. 4.6. Using these circuits the steady state dq-equations are written with motor reference currents i.e., positive currents flowing into the machine:

$$0 = R_i I_{\mathrm{d}i} - \omega_{\mathrm{sle}} L_{\mathrm{e}i} I_{\mathrm{q}i} - \omega_{\mathrm{sle}} \lambda_{\mathrm{q}i} \tag{4.8}$$

$$0 = R_i I_{\mathrm{q}i} + \omega_{\mathrm{sle}} L_{\mathrm{e}i} I_{\mathrm{d}i} + \omega_{\mathrm{sle}} \lambda_{\mathrm{d}i} \tag{4.9}$$

with the wound rotor d- and q-axis currents given by $I_{\mathrm{d}i}$ and $I_{\mathrm{q}i}$ respectively. dq flux linkages are given by $\lambda_{\mathrm{d}i}$ and $\lambda_{\mathrm{q}i}$, and the per phase winding resistance is given by R_i. $L_{\mathrm{e}i}$ is the per phase end winding inductance. Both R_i and $L_{\mathrm{e}i}$ are calculated using the equations given in Appendix A. The electrical slip speed ω_{sle} is defined as $\omega_{\mathrm{sle}} = \omega_{\mathrm{m}} - \omega_{\mathrm{r}}$ (in electrical rad/s). ω_{r} is the output wound rotor speed and ω_{m} is the input PM rotor speed. Further analysis requires

the dq inductances to be defined. It is important that the mutual inductances between the 30 different phases should be taken into account, as is done in [17]. Taking into consideration the d-axis flux linkage, and thus also inductance, the flux linkage is written as (for $i = 1$):

$$\begin{aligned}\lambda_{\mathrm{d1}} =& L_{\mathrm{d(1,1)}} I_{\mathrm{d1}} + L_{\mathrm{d(1,2)}} I_{\mathrm{d2}} + ... \\ &+ L_{\mathrm{d(1,9)}} I_{\mathrm{d9}} + L_{\mathrm{d(1,10)}} I_{\mathrm{d10}} + \lambda_{\mathrm{m1}}\end{aligned} \tag{4.10}$$

where $L_{\mathrm{d(1,1)}}$ is the circuit self inductance for set $i = 1$. $L_{\mathrm{d(1,2)}}$ to $L_{\mathrm{d(1,10)}}$ are mutual inductances between circuit $i = 1$ and circuits $i = 2$ to 10. Note that these equations only consider the active stack, and not the end windings. λ_{m1} is the PM flux linkage contribution.

Equations (4.1) and (4.3) indicate that all currents in the upper layer are equal and all currents in the lower layer are equal. Thus combining (4.10) with (4.1) and (4.3), we write

$$\begin{aligned}\lambda_{\mathrm{d1}} =& (L_{\mathrm{d(1,1)}} + L_{\mathrm{d(1,3)}} + ... + L_{\mathrm{d(1,9)}}) I_{\mathrm{d1}} \\ &+ (L_{\mathrm{d(1,2)}} + L_{\mathrm{d(1,4)}} + ... + L_{\mathrm{d(1,10)}}) I_{\mathrm{d2}} + \lambda_{\mathrm{m1}} \\ =& L_{\mathrm{d1(upper)}} I_{\mathrm{d1}} + L_{\mathrm{d1(lower)}} I_{\mathrm{d2}} + \lambda_{\mathrm{m1}} \\ \approx& L_{\mathrm{d1}} I_{\mathrm{d1}} + \lambda_{\mathrm{m1}} \quad (\text{assume } I_{\mathrm{d1}} \approx I_{\mathrm{d2}})\end{aligned} \tag{4.11}$$

where $L_{\mathrm{d1}} = L_{\mathrm{d1(upper)}} + L_{\mathrm{d1(lower)}}$, which is the total inductance of set $i = 1$. $L_{\mathrm{d1(upper)}}$ and $L_{\mathrm{d1(lower)}}$ are the upper layer and lower layer inductance contributions, respectively. Note that the assumption must be made that $I_{\mathrm{d1}} \approx I_{\mathrm{d2}}$, which is not necessarily correct. A percentage difference in current magnitudes exists between the two layers, but this assumption allows us to use a powerful analysis method which yields very accurate results (as will be shown later), justifying the assumption.

The q axis inductance can also be determined using the above method. The generic flux linkage equations are written as

$$\lambda_{\mathrm{d}i} = L_{\mathrm{d}i} I_{\mathrm{d}i} + \lambda_{\mathrm{m}i} \tag{4.12}$$

$$\lambda_{\mathrm{q}i} = L_{\mathrm{q}i} I_{\mathrm{q}i}. \tag{4.13}$$

The d- and q-axis inductances are given by $L_{\mathrm{d}i}$ and $L_{\mathrm{q}i}$, with the PM flux linkage contribution given by $\lambda_{\mathrm{m}i}$ for set i.

It is required that the voltage equations be written in terms of $L_{\mathrm{d}i}$, $L_{\mathrm{q}i}$ and $\lambda_{\mathrm{m}i}$. This is done by combining (4.12) and (4.13) with (4.8) and (4.9):

$$0 = R_i I_{\mathrm{d}i} - \omega_{\mathrm{sle}} L_{ei} I_{\mathrm{q}i} - \omega_{\mathrm{sle}} L_{\mathrm{q}i} I_{\mathrm{q}i} \tag{4.14}$$

$$0 = R_i I_{\mathrm{q}i} + \omega_{\mathrm{sle}} L_{ei} I_{\mathrm{d}i} + \omega_{\mathrm{sle}} L_{\mathrm{d}i} I_{\mathrm{d}i} + \omega_{\mathrm{sle}} \lambda_{\mathrm{m}i}. \tag{4.15}$$

It is further required that (4.14) and (4.15) be rewritten to give the dq currents in terms of $L_{\mathrm{d}i}$, $L_{\mathrm{q}i}$ and $\lambda_{\mathrm{m}i}$ (based on a method detailed in [7] and [9]). To achieve this (4.14) and (4.15) are written with $I_{\mathrm{d}i}$ and $I_{\mathrm{q}i}$, respectively, as the subjects. The resulting equations are cross substituted to yield the following equations for $I_{\mathrm{d}i}$ and $I_{\mathrm{q}i}$:

$$I_{\mathrm{d}i} = \frac{-{\omega_{\mathrm{sle}}}^2 (L_{\mathrm{q}i} + L_{ei}) \lambda_{\mathrm{m}i}}{{R_i}^2 + {\omega_{\mathrm{sle}}}^2 (L_{\mathrm{q}i} + L_{ei})(L_{\mathrm{d}i} + L_{ei})} \tag{4.16}$$

$$I_{\mathrm{q}i} = \frac{-\omega_{\mathrm{sle}} R_i \lambda_{\mathrm{m}i}}{{R_i}^2 + {\omega_{\mathrm{sle}}}^2 (L_{\mathrm{q}i} + L_{ei})(L_{\mathrm{d}i} + L_{ei})}. \tag{4.17}$$

Performance parameters of the slip coupler must also be calculated. The torque is calculated using the following equation:

$$T = \sum_{i=1}^{N_{\mathrm{ph}}/3} \frac{3}{2} \left(\frac{p}{2}\right) (\lambda_{\mathrm{d}i} I_{\mathrm{q}i} - \lambda_{\mathrm{q}i} I_{\mathrm{d}i}). \tag{4.18}$$

Conductor losses in the wound rotor coils are calculated using

$$P_{\mathrm{co}} = T\omega_{\mathrm{sl}} = \sum_{i=1}^{N_{\mathrm{ph}}/3} 3 I_{\mathrm{RMS}i}^2 R_i \tag{4.19}$$

where

$$I_{\mathrm{RMS}i} = \sqrt{\frac{{I_{\mathrm{d}i}}^2 + {I_{\mathrm{q}i}}^2}{2}}. \tag{4.20}$$

$I_{\mathrm{RMS}i}$ is the RMS phase current for set i. Note that conductor losses will be the only real losses in the slip coupler, since core losses (eddy current and hysteresis) at such low frequencies, in this case 4.2 Hz at rated conditions, are neglected. Friction and windage losses are also neglected since bearing friction will only apply to a slip speed of 18 r/min, which is very slow. Windage, when calculated using a formula given in [20], is found to be less than 1 W, and thus has almost no impact on efficiency. Finally, efficiency can be written as

$$\eta = \frac{P_{\mathrm{in}} - P_{\mathrm{co}}}{P_{\mathrm{in}}}. \tag{4.21}$$

where

$$P_{\text{in}} = T\omega_{\text{in}}. \tag{4.22}$$

ω_{in} is the input mechanical speed (in rad/s) of the PM rotor.

4.4 Simulation Procedure Using FEM

The slip coupler operates on the same principles as induction machines. Like in induction machines, the current magnitude and angle for a given slip value are not known, and since no control is being used on the machine the current phasor cannot be prescribed or forced. Thus the current phasor must be determined iteratively for a given slip value. This can easily be done using a transient FE simulation, which not only determines the transient response, but also the current phasors and induced torque at steady state for a given operating point. However, a transient FE simulation tends to be relatively slow.

In this study a time stepped, static FE simulation is used along with the proposed analysis method. As such the current phasors at a given operating point are not known, and a series of static FE simulations are run iteratively to evaluate machine performance at the operating point. Two potential iterative methods are evaluated, both of which yield the same results, but at different convergence rates. In both methods the rated torque T_{rated}, slip s and operating speed are known, and used as input variables.

Note that to obtain correct performance parameters the calculations detailed must be repeated for each set $i = 1, 2, \ldots, 10$. However, since (4.1) and (4.2) states that all upper layer dq currents are equal, and (4.3) and (4.4) states that all lower layer dq currents are equal, only $i = 1, 2$ needs to be calculated. The results are then replicated to $i = 3, 4, ...N_{\text{ph}}/3$.

4.4.1 Method 1

The first method evaluated is given by [17]. The method is used to calculate the current phasors iteratively, in terms of flux linkage:

1. Since T_{rated} and s are known, P_{co} is calculated using (4.19). $I_{\text{RMS}i}$ is calculated, also using (4.19). It is assumed that conductor losses are equal in all phases.

2. Set $I_{qi} = \sqrt{2}I_{RMSi}$ and $I_{di} = 0$. These are used as initial starting values for dq currents. (4.5) is used to transform the currents to the phase domain. The first FE simulation is run for $i = 1, 2, \ldots, 10$, using $\mathbf{I}_{abc(i)}$ as input.
3. The FE simulation provides $\boldsymbol{\lambda}_{abc(i)}$ as output, which is transformed using (4.7) to attain $\boldsymbol{\lambda}_{dq(i)}$ (λ_{di} and λ_{qi}).
4. New values for I_{di} and I_{qi} are calculated using (4.8) and (4.9), with λ_{di} and λ_{qi} as input. Note that the previous iteration values for I_{di} and I_{qi} are used to calculate the $\omega_{sle}L_{ei}I_{di}$ and $\omega_{sle}L_{ei}I_{qi}$ terms.
5. Using (4.5) I_{di} and I_{qi} are converted to the phase domain. The next FE simulation is run.
6. The last three steps are repeated until convergence of both the upper and lower layer currents occurs.

4.4.2 Method 2

The second method evaluated is used in [17] and [8]. The method is also used to calculate the current phasors iteratively, but this time in terms of L_{di}, L_{qi} and λ_{mi}:

1. Since T_{rated} and s are known, P_{co} is calculated using (4.19). I_{RMSi} is calculated, also using (4.19). It is assumed that conductor losses at this point are equal in all phases.
2. Set $I_{qi} = \sqrt{2}I_{RMSi}$ and $I_{di} = 0$. These are used as initial starting values for dq currents. (4.5) is used to transform the currents to the phase domain. The first FE simulation is run for $i = 1, 2, \ldots, 10$, using $\mathbf{I}_{abc(i)}$ as input.
3. The FE simulation provides $\boldsymbol{\lambda}_{abc(i)}$ as output, which is transformed using (4.7) to attain $\boldsymbol{\lambda}_{dq(i)}$ (λ_{di} and λ_{qi}).
4. Using (4.12), and with a d-axis current value of 0 (PM flux linkage is the only flux linkage component present on d-axis), λ_{mi} is assigned the value of λ_{di}
5. Using (4.13), L_{qi} is calculated. L_{di} is estimated to have a value similar to L_{qi}, and thus for the second iteration $L_{di} = L_{qi}$.

6. New values for $I_{\mathrm{d}i}$ and $I_{\mathrm{q}i}$ are calculated using (4.16) and (4.17). Using (4.5) $I_{\mathrm{d}i}$ and $I_{\mathrm{q}i}$ are transformed to the phase domain. The next FE simulation is run.
7. The FE simulation provides $\boldsymbol{\lambda}_{\mathrm{abc}(i)}$ as output, which is transformed using (4.7) to attain $\boldsymbol{\lambda}_{\mathrm{dq}(i)}$. Using (4.12) and (4.13) along with $\lambda_{\mathrm{d}i}$ and $\lambda_{\mathrm{q}i}$, new values for $L_{\mathrm{d}i}$ and $L_{\mathrm{q}i}$ are calculated. The value calculated for $\lambda_{\mathrm{m}i}$ in the first iteration is used.
8. New values for $I_{\mathrm{d}i}$ and $I_{\mathrm{q}i}$ are calculated using (4.16) and (4.17), with $L_{\mathrm{d}i}$, $L_{\mathrm{q}i}$ and $\lambda_{\mathrm{m}i}$ as input.
9. Using (4.5), $I_{\mathrm{d}i}$ and $I_{\mathrm{q}i}$ are converted to the phase domain. The next FE simulation is run.
10. The last three steps are repeated until convergence of both the upper and lower layer currents occurs.

The methods described above are both used to determine the operating point of the slip coupler for a given slip value iteratively, by determining the current phasors, as well as the flux linkages for the various phases. The performance of the machine is evaluated using the currents and flux linkages. The main

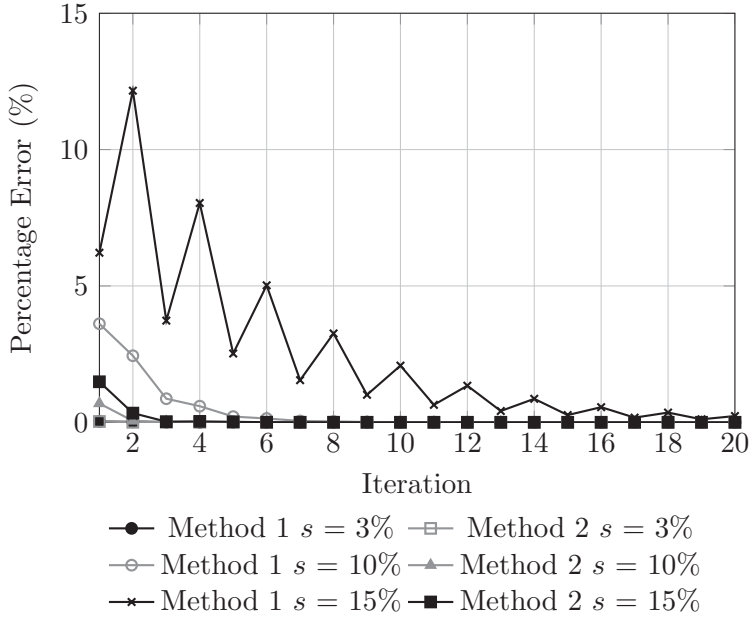

Figure 4.7: Convergence rate of upper layer coil currents using methods 1 and 2 for slip $s = 3, 10$ and 15% [17]

performance characteristics are torque and efficiency which are determined using (4.18) and (4.21).

For comparison the same slip coupler model is solved using both methods described, over a range of slip values. The results of the comparison are given in Fig. 4.7.

Both methods converge to the same values for a given operating point, but as can be seen in Fig. 4.7, the amount of iterations until convergence differs greatly between the two methods. Method 2, when used within the slip range of 0 to 20%, has a far superior convergence rate, with four FE simulations or fewer required for convergence. When using method 2 convergence occurs within two iterations at rated slip of 3% and within three iterations at 15% slip. Method 1 also converges within two iterations at rated slip, but has a much slower convergence rate when evaluating at higher slip values, with more than twenty iterations required at 15% slip. Based on these results, method 2 is chosen for the optimisation process detailed in this chapter.

4.5 Optimisation of Slip Coupler

The design requirements are fairly straightforward, since the machine acts as a coupling and only needs to transfer torque. The required torque (T_{rated}) is 35 Nm, at a rated output speed (N_{out}) of 600 r/min and a rated slip (s) of 0.03. All other performance requirements and input variables can be calculated from these parameters.

A set of machine dimensions is used as variables by the optimisation suite *VisualDoc*. These machine dimensions are given as input variables to the FEM package. The performance of the slip coupler, under the given input variables, is provided as output from the FEM package. In this case an in-house FE package is used, called *SEMFEM*. A *SEMFEM* script is used, with method 2 described in Section 4.4 executed in this script. The performance output provided by *SEMFEM* is then used by the optimisation suite to evaluate the current iteration, and to determine the new values of the input variables for the next iteration. The optimisation process is illustrated in Fig. 4.8.

The optimisation suite receives various performance metrics as output from the FE package and uses this information to determine the dimensions of the next optimisation iteration to be evaluated (each optimisation iteration consists

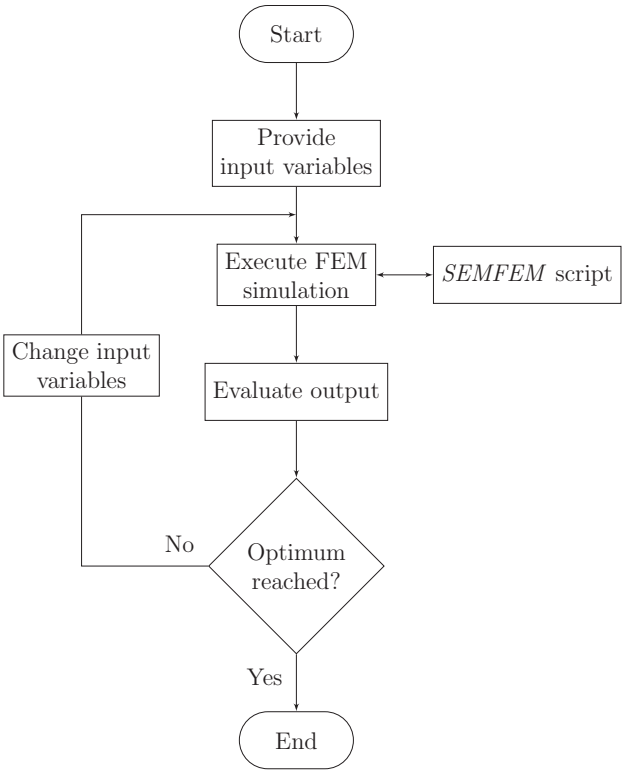

Figure 4.8: Flow diagram of the *VisualDoc* optimisation process

of up to four static FE simulations, as per method 2 described above). This process is repeated until an optimised model is attained.

The optimisation is kept relatively simple, with only eight dimensional variables available to the optimiser, as shown in Fig. 4.9 and Table 4.1. The eighth variable, namely the axial length, is not shown in Fig. 4.9. The objective function is chosen to be active mass, and this is minimised, subject to the constraints given in Table 4.2.

4.6 Optimisation Results

The optimisation of the slip coupler is completed using *VisualDoc*, with the MMFD (modified method of feasible direction) algorithm used as the primary optimisation algorithm. The results can be seen in Table 4.1. The dimensional variables used during the optimisation process are given, along with their near optimal values. The minimised value of the objective function, active mass, is also given.

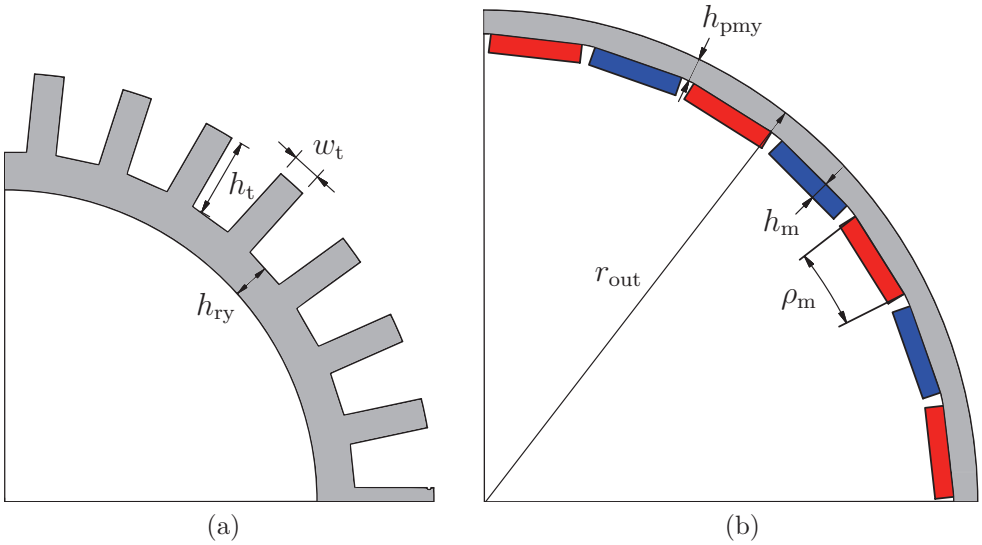

Figure 4.9: Dimensions used as optimisation input variables

Table 4.1: Design variables and optimised values for slip coupler

Fixed Input	**Value**
Output Speed	600 r/min
Rated Slip	0.03
Optimisation Variables	**Optimised Value**
Axial Length - l_a	65 mm
Tooth Height - h_t	17.3 mm
Tooth Width - w_t	6.4 mm
Wound Rotor Yoke - h_{ry}	8 mm
Magnet Height - h_m	4 mm
Magnet Pitch - ρ_m	87%
PM Rotor Yoke - h_{pmy}	5 mm
Outside Radius - r_{out}	105 mm
Objective Function	**Optimised Value**
Active Mass (minimised)	7 kg

An active mass of 7 kg was attained, which is favourable, but excludes any additional mounting fittings. A total magnet mass of 880 g was achieved, which is also quite favourable. The outer diameter of 210 mm is considerably larger than the stack length of 65 mm, implying that the slip coupler is an axially short but radially large machine, similar to low speed, direct drive machines.

The final values of the parameters constrained during the optimisation are given in Table 4.2, with the constraint limits also shown. All of the constraints

Table 4.2: Optimisation constraints for slip coupler

Constraint (at rated slip)	Limits	Values
Generated Torque	$34 < T < 36$ Nm	34.9 Nm
Torque Ripple	$< 3\%$	1.4%
Efficiency	$96.9\% < \eta < 97.1\%$	97%
Current Density	< 4 A/mm^2	2.72 A/mm^2

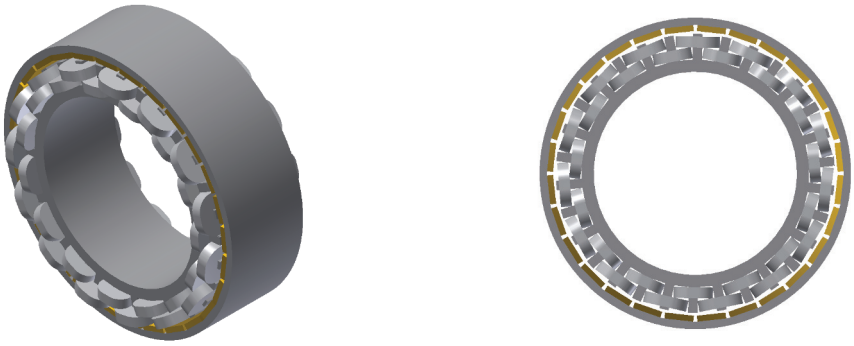

(a) (b)

Figure 4.10: A CAD representation of the active components of the slip coupler assembly, without any mounting fixtures shown.

are met quite comfortably, with torque ripple especially low, as is expected from a 28/30 pole/slot combination. The efficiency is exactly 97%, since only conductor losses are considered.

4.7 Slip Coupler Prototype Construction

4.7.1 Design of Mounting Fixtures

The optimisation process determined the exact design dimensions of the active components of the slip coupler. These components are illustrated in Fig. 4.10. The machine is obviously not useful in such a basic state, and requires several mounting fixtures and/or a casing to be able to connect input and output shafts (bearing in mind that the slip coupler only transfers torque from one shaft to another).

An important design consideration is the fact that the slip coupler contains permanent magnets, which means that during assembly and operation radial forces are present which attract the wound rotor steel to the PM rotor. This

magnetic pull causes serious issues with alignment, and to this end the slip coupler is designed with an internal hub assembly, to facilitate the alignment. The hub consists of two independently rotating segments, connected via bearings, to allow the wound rotor and PM rotor to rotate independently and not transfer any torque mechanically.

The laminations for both the wound and PM rotor are stacked onto rods which are connected to end plates. These end plates are connected internally to the hub assembly, and externally to interchangeable couplings. The coupling are used to connect the input and output shafts to the slip coupler. This design is illustrated in Fig. 4.11.

Most of the prototype is constructed easily by simply stacking laminations and fastening various nuts and bolts. There are some aspects that require somewhat more effort, and these are discussed in more detail in the following section.

4.7.2 Prototype Construction

The laminations are stacked onto rods and fastened onto end plates, as mentioned earlier. The conductors and magnets are then applied to the various sections. The conductors used in this prototype consist of 1.6 mm thick 1050A aluminium plates, laser cut into the desired shape. The plates used are shown in Figs. 4.12a and 4.12b. The magnets are N48H-grade neodymium iron boron magnets, shown in Fig. 4.12c.

The magnets are glued onto the PM rotor laminations using an industrial grade epoxy. Initially all the magnets with the same polarity are glued and clamped into place, and thereafter the opposite polarity magnets are glued in between. This process is shown in Fig. 4.13.

The wound rotor is constructed by stacking the aluminium plates onto the teeth present on the laminations. This is done by hand, and is a very simple method to add conductors onto the rotor. The plates are held in place by adding a wedge at the top of each tooth opening. The stacked plates, as well as the wedges, are shown in Fig. 4.14.

With the construction of the two halves complete, as shown in Fig. 4.15, the final assembly of the slip coupler can be done.

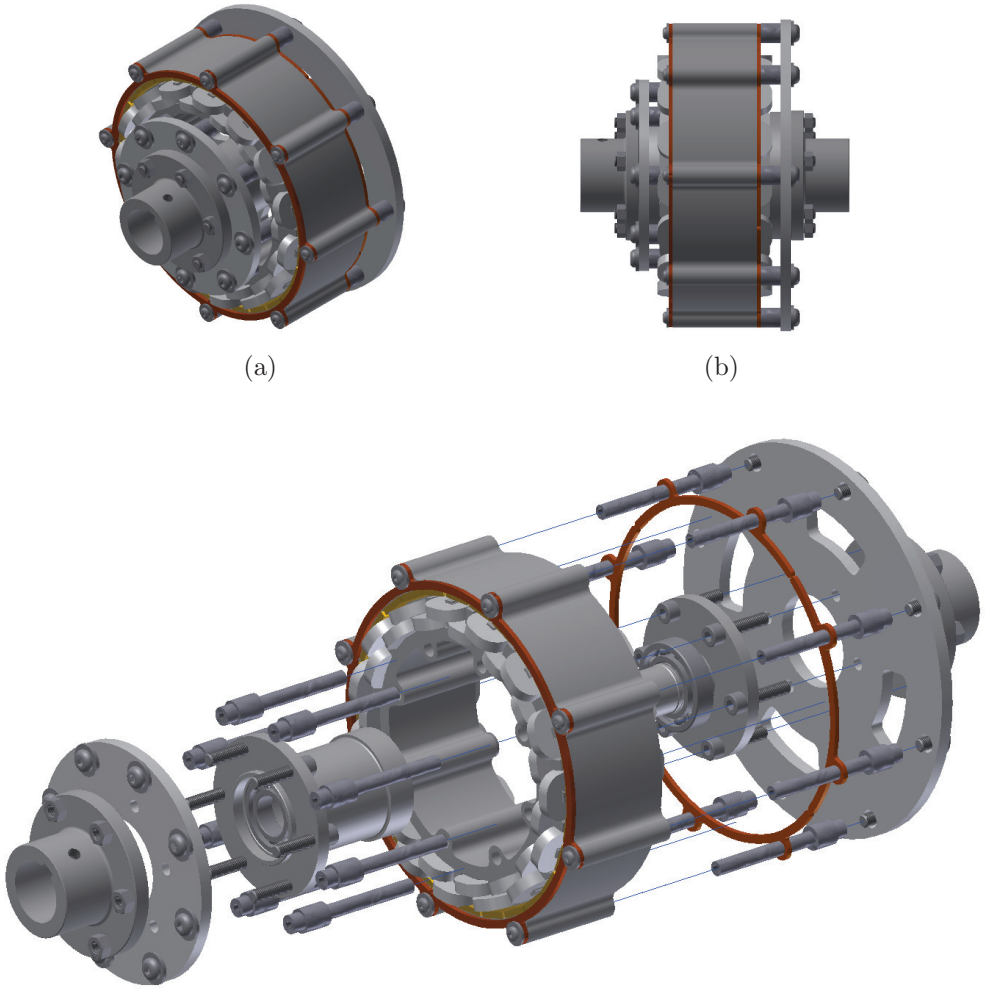

(a) (b)

(c)

Figure 4.11: A CAD representation of the final assembly of the slip coupler, including all mounting fixtures. An exploded view is also given in (c).

(a) (b) (c)

Figure 4.12: The active conductor components of the slip coupler, with (a) a single aluminium plate and (b) a stack of aluminium plates shown. A magnet used in the prototype is shown in (c).

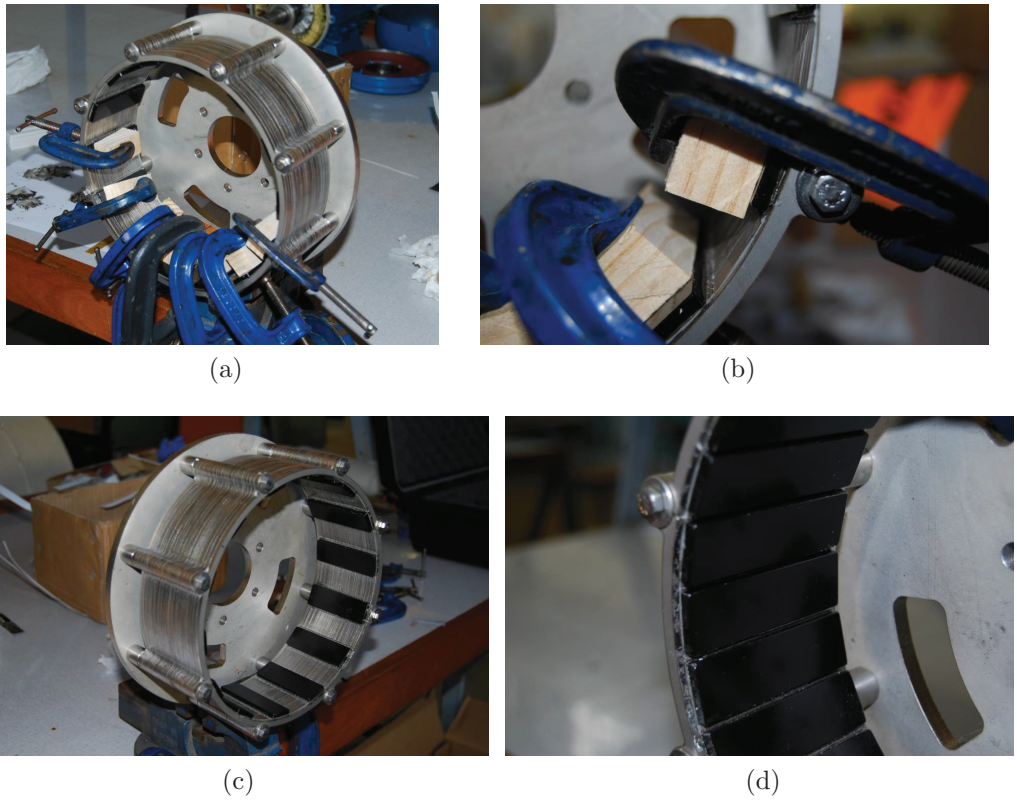

(a) (b)

(c) (d)

Figure 4.13: Photos detailing the construction of the PM rotor, with (a) the magnet gluing process shown and (b) a close-up of the applied clamps. The laminations with only the north polarised magnets is shown in (c), as well as the finished product in (d).

4.7.3 Final Assembly

The final assembly is completed by fixing the hub assembly to the PM rotor, and then lowering the wound rotor into place inside the PM rotor. This process is shown in Fig. 4.16. Note that the wound rotor is lowered into place using a block and tackle system, since the wound rotor must be lowered into place gently to avoid being damaged by the extreme pull of the magnets.

Once the wound rotor is lowered onto the PM rotor and hub, all bolts are fastened and the prototype is removed from the mounting stand. Finally, the mechanical couplings are attached to both sides of the prototype, as shown in Fig. 4.16e, to allow the connection of input and output shafts. This final prototype assembly is used for lab testing.

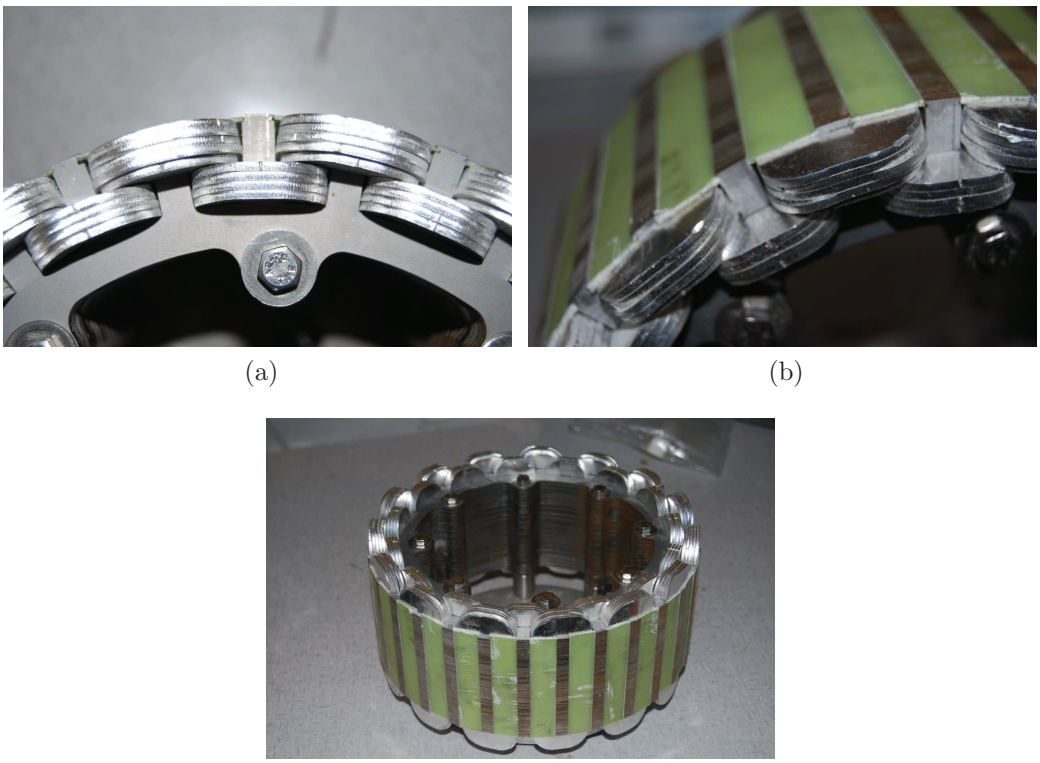

(a) (b)

(c)

Figure 4.14: The wound rotor during construction, with (a) a close-up of the stacked aluminium plates, which are the conductor coils. The (b) wedges used to keep the plates in place are shown, as well as (c) the final rotor construction.

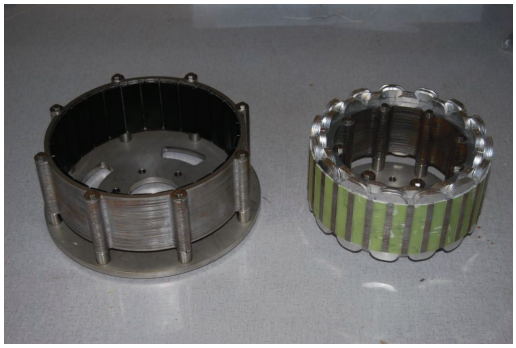

Figure 4.15: The fully constructed two halves of the slip coupler.

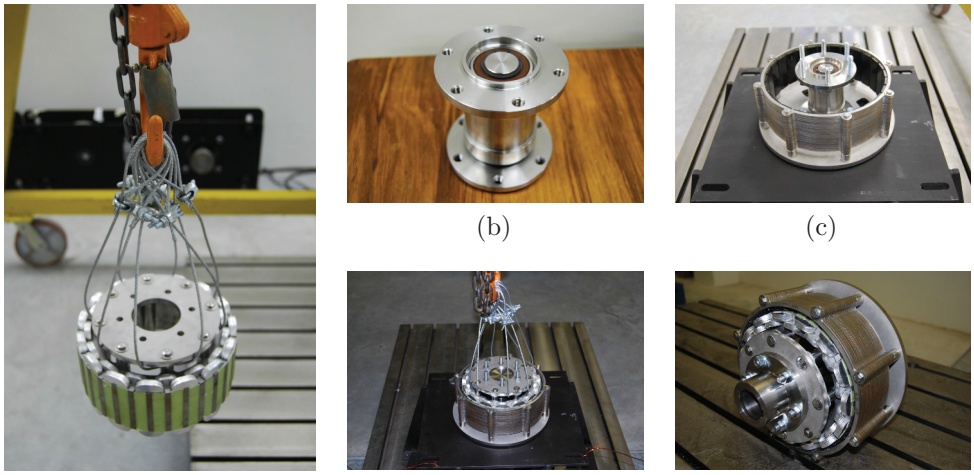

(a) (b) (c) (d) (e)

Figure 4.16: The final assembly, with (a) the wound rotor on a block and tackle, (b) the hub assembly, (c) the PM rotor attached to a mounting platform, (d) the wound rotor being lowered into place and (e) the completed slip coupler prototype.

4.8 Chapter Summary

In this chapter a complete slip coupler prototype is designed and optimised using static, time stepped FE simulations. The optimisation process is detailed, and a machine prototype is constructed from the optimised design. The optimised machine produces 34.9 Nm of torque, has a torque ripple of 1.4%, and an efficiency of 97%, all at a rated slip of 3%. The active mass of the machine is 7 kg. The construction and assembly process of the prototype is shown. The prototype is constructed with the intention of laboratory testing the machine.

Chapter 5

Design of PMSG

The final component in the proposed drive train is the permanent magnet synchronous generator (PMSG), as highlighted in Fig. 5.1. The generator is directly grid-connected, which means that little or no power electronics are used to control the generator. In this chapter the design of a PMSG, which is intended to be used on the proposed drive train, is detailed. Design optimisation is done to get the smallest and lightest design, and simulation results of the optimised design are compared between two different FE packages, in order to verify that the design works as intended. A prototype of the optimised design is not built, since PMSGs have been thoroughly researched in the past. In this study the focus is more on the experimental verification of the slip coupler design; the PMSG design is only included to give a complete picture of the proposed drive train.

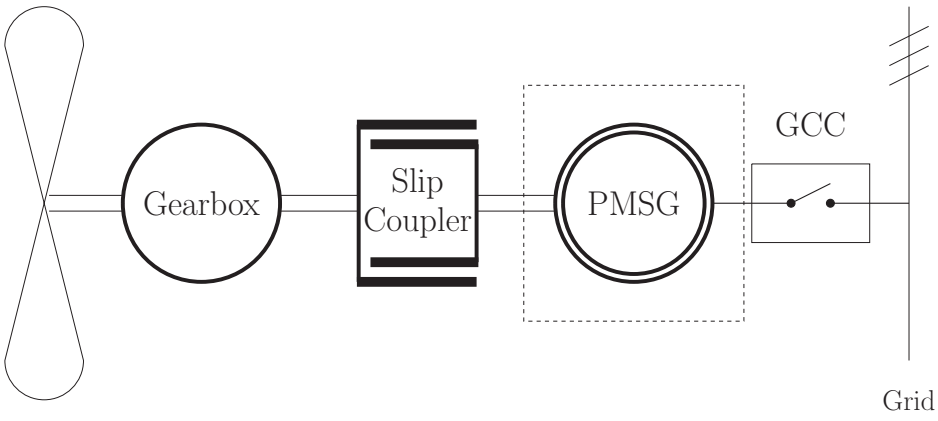

Figure 5.1: The proposed drive train topology, with the PMSG highlighted.

5.1 Directly Grid-Connected PMSG

The primary design consideration for the PMSG is the requirement to be directly grid-connected, thereby eliminating the need for a power converter and/or controller. This has the advantage of removing converter losses from the system as well as removing the risk of turbine downtime due to converter failure. Grid-connected synchronous generators are limited to only run at a fixed speed, as prescribed by the grid frequency and the number of poles.

The PMSG will have a very simple electronic switch to connect to the grid, called a grid connection controller (GCC), which is shown in Fig. 5.1. The GCC monitors the machine speed, and once the wind speed is sufficient to allow the PMSG to run close to synchronous speed, the GCC synchronises the PMSG with the grid, thereby forcing a constant 50 Hz frequency in the PMSG. If the wind speed drops low enough for the PMSG to no longer generate power, the GCC also disconnects the PMSG from the grid.

FE simulations are more difficult for grid-connected PMSGs than for normal power-controlled PMSGs. The only known electrical quantity is the magnitude of the grid voltage, which is fixed at 230 V (RMS, line-to-line). The current phasor is unknown, and cannot be forced since the current position is dependent on both the machine design and the fixed grid voltage. This complicates matters when the FE package can only use current phasors as input, as is the case here. Thus an iterative approach is used to determine the current and voltage phasors relative to the machine. The current magnitude is determined by using copper losses as an input variable, thereby simulating an external load.

The PMSG design detailed in this chapter consists of a 10/12 pole/slot combination, with permanent magnets on the rotor to provide the magnetic field. The synchronous speed is 600 rpm, rated output power 2.2 kW and rated input torque around 36.5 Nm (with a desired efficiency of 93%). The stator consists of double layer, non-overlap copper windings, which is a relatively simple design. The PMSG will be fitted inside the casing of an existing motor, thereby forcing an outer diameter of 185 mm, and a stack length of no more than 140 mm.

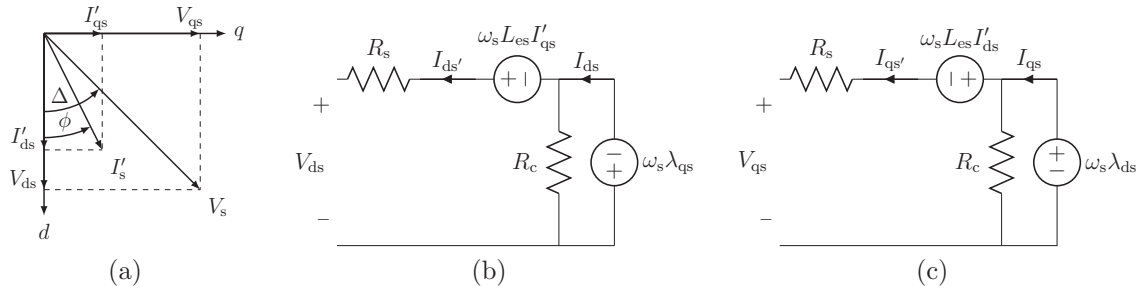

Figure 5.2: Equivalent circuit diagrams of the PMSG, with (a) the vector diagram for the dq currents and voltages, (b) d-axis equivalent circuit, and (c) q-axis equivalent circuit.

5.2 PMSG Equivalent Model

The dq equivalent circuits for the PMSG are given in Fig. 5.2. In these circuits the core loss resistance (R_c) is set in parallel with the voltage contribution of the dq flux linkages ($\omega_s \lambda_{qs}$ and $\omega_s \lambda_{ds}$), while the voltage contribution from the end-winding inductances ($\omega_s L_{es} I'_{qs}$ and $\omega_s L_{es} I'_{ds}$) is in series with the parallel circuit and the winding resistance (R_s). Using these circuits, the equations for the d- and q-axis voltages can respectively be written as

$$V_{ds} = -R_s I'_{ds} + \omega_s L_{es} I'_{qs} - \omega_s \lambda_{qs} \tag{5.1}$$

$$V_{qs} = -R_s I'_{qs} - \omega_s L_{es} I'_{ds} + \omega_s \lambda_{ds}, \tag{5.2}$$

with I'_{ds} and I'_{qs} being the total d- and q-axis currents of the series circuits. As mentioned earlier, R_s is the per phase resistance of the copper windings on the stator, and L_{es} is the per phase end winding leakage inductance. The equations used to calculate R_s and L_{es} are given in Appendix A. The synchronous speed, in electrical rad/s, is given by ω_s. The outputs of the FE simulation are the d- and q-axis flux linkages, given by λ_{ds} and λ_{qs}, respectively. The inputs to the FE package are the d- and q-axis currents in the parallel sections of the circuits, I_{ds} and I_{qs}, which are given by

$$I_{ds} = I'_{ds} - \frac{\omega_s \lambda_{qs}}{R_c} \tag{5.3}$$

$$I_{qs} = I'_{qs} + \frac{\omega_s \lambda_{ds}}{R_c}, \tag{5.4}$$

respectively. R_c is the stator iron (or core) loss resistance. The equations used to calculate R_c are given in Appendix A. The dq flux linkages are defined as

$$\lambda_{ds} = -L_{ds} I_{ds} + \lambda_{ms} \tag{5.5}$$

$$\lambda_{\mathrm{qs}} = -L_{\mathrm{qs}} I_{\mathrm{qs}}, \tag{5.6}$$

with L_{ds} and L_{qs} being the d- and q-axis inductances, respectively. λ_{ms} is the flux linkage contribution of the permanent magnets. For the purposes of this study, it is required that the voltage equations of Eq. (5.1) and Eq. (5.2) be rewritten in terms of current:

$$I'_{\mathrm{ds}} = \frac{-V_{\mathrm{ds}} + \omega_{\mathrm{s}} L_{\mathrm{es}} I'_{\mathrm{qs}} - \omega_{\mathrm{s}} \lambda_{\mathrm{qs}}}{R_{\mathrm{s}}} \tag{5.7}$$

$$I'_{\mathrm{qs}} = \frac{-V_{\mathrm{qs}} - \omega_{\mathrm{s}} L_{\mathrm{es}} I'_{\mathrm{ds}} + \omega_{\mathrm{s}} \lambda_{\mathrm{ds}}}{R_{\mathrm{s}}}. \tag{5.8}$$

The peak line-to-neutral voltage at the PMSG terminals, V_{s}, is related to its dq voltage components through

$$\begin{bmatrix} V_{\mathrm{ds}} \\ V_{\mathrm{qs}} \end{bmatrix} = V_{\mathrm{s}} \begin{bmatrix} \cos(\Delta) \\ \sin(\Delta) \end{bmatrix} \tag{5.9}$$

$$\Delta = \arctan\left(\frac{V_{\mathrm{qs}}}{V_{\mathrm{ds}}}\right) \tag{5.10}$$

where Δ is the angle between V_{s} and the d-axis. Similarly, the peak line current at the PMSG terminals, I'_{s}, is related to its dq current components through

$$\begin{bmatrix} I'_{\mathrm{ds}} \\ I'_{\mathrm{qs}} \end{bmatrix} = I'_{\mathrm{s}} \begin{bmatrix} \cos(\phi) \\ \sin(\phi) \end{bmatrix} \tag{5.11}$$

$$\phi = \arctan\left(\frac{I'_{\mathrm{qs}}}{I'_{\mathrm{ds}}}\right) \tag{5.12}$$

where ϕ is the angle between I'_{s} and the d-axis. The performance of the PMSG is also evaluated. The generated torque is given by

$$T = \left(\frac{3}{2}\right)\left(\frac{p}{2}\right)(\lambda_{\mathrm{ds}} I_{\mathrm{qs}} - \lambda_{\mathrm{qs}} I_{\mathrm{ds}}) \tag{5.13}$$

with p the number of poles. The apparent output power and real output power are given, respectively, as

$$S = \frac{3}{2} V_{\mathrm{s}} I'_{\mathrm{s}} \tag{5.14}$$

$$P_{\mathrm{out}} = \frac{3}{2} V_{\mathrm{s}} I'_{\mathrm{s}} \cos(\theta) = P_{\mathrm{mech}} - P_{\mathrm{losses}} \tag{5.15}$$

with

$$\theta = \phi - \Delta \tag{5.16}$$

$$P_{\text{mech}} = P_{\text{in}} = T\omega_{\text{s}}. \tag{5.17}$$

P_{losses} consists of copper losses (P_{cus}), stator core losses (P_{c}) and friction and windage losses (P_{fw}). Iron losses (eddy current and hysteresis losses) in the conductors, rotor and permanent magnets are assumed to be negligible, and this assumption is verified by FEM simulations. P_{cus} is given by

$$P_{\text{cus}} = \frac{3}{2} I_{\text{s}}'^2 R_{\text{s}}. \tag{5.18}$$

The equation used to calculate P_{c} is given in Appendix A, using a method described in [21]. P_{fw} is calculated using a formula given in [20], but these losses were found to be so small as to be almost negligible. Incorporating all these losses, the efficiency can be written as

$$\eta = \frac{P_{\text{in}} - P_{\text{losses}}}{P_{\text{in}}}. \tag{5.19}$$

The transformations used in this analysis are given by

$$\mathbf{I}_{\text{abc}} = \mathbf{K}_{\text{p}}(\alpha)\mathbf{I}_{\text{dq}} \tag{5.20}$$

$$\boldsymbol{\lambda}_{\text{dq}} = \mathbf{K}_{\text{p}}^{-1}(\alpha)\boldsymbol{\lambda}_{\text{abc}}. \tag{5.21}$$

where $\mathbf{K}_{\text{p}}$ is Park's transformation and α is the electrical angle between the rotor direct axis and the phase a axis. This concludes the set of useful equations for analysis of the PMSG.

5.3 FE Simulation Procedure

The PMSG is directly grid-connected, which in this case means that the output terminals of the PMSG are connected to a fixed voltage supply of 400 V (RMS, line-to-line), or 230 V (RMS, line-to-neutral). Thus no drive is present to control the PMSG, which has a significant impact on the operation and specifically the power factor of the PMSG. The PMSG is evaluated at a rated speed of 600 r/min and a frequency of 50 Hz.

The PMSG operating point is simulated using an iterative method, with a fixed voltage applied at the terminals and a rated current calculated from rated copper losses (using (5.18)). The following procedure is used to determine the operating point and performance metrics of the PMSG, using time-stepped, static FE simulations:

1. The rated current I_s is calculated using (5.18) (it is assumed that $I_s = I'_s$ for the input current), with P_{cus} chosen as an input variable.
2. Set initial starting values of dq currents, by setting $I_{qs} = I_s$ and $I_{ds} = 0$. Transform to the phase domain using (5.20). Using $\mathbf{I}_{abc}$ as input, run first FE simulation.
3. $\boldsymbol{\lambda}_{abc}$ is received as output from the FE package. This is transformed to dq flux linkages using (5.21) to get λ_{ds} and λ_{qs}.
4. $I_{qs'}$ and $I_{ds'}$ are calculated using (5.3) and (5.4), with R_c calculated using the equations given in Appendix A.
5. V_{qs} and V_{ds} are calculated using (5.1) and (5.2).
6. Δ is calculated using (5.10). With $V_s = \sqrt{2} \times 230$ V (325.3 V), new values for V_{qs} and V_{ds} are calculated using (5.9).
7. New values for $I_{qs'}$ and $I_{ds'}$ are calculated using (5.7) and (5.8).
8. ϕ is calculated using (5.12). With I_s as calculated in step 1, the final values for $I_{qs'}$ and $I_{ds'}$ are calculated using (5.11).
9. These final values for $I_{qs'}$ and $I_{ds'}$ are used together with (5.3) and (5.4) to calculate new values for I_{qs} and I_{ds}, which will be used as input for the next FE iteration.
10. I_{qs} and I_{ds} are transformed to the phase domain using (5.20), and used as input for the next FE iteration.
11. The previous eight steps are repeated until convergence of the currents and voltages are achieved, which is usually within five to six FE iterations.

This iterative method is used to determine the operating point and performance characteristics of the PMSG for given input variables during the optimisation process. Note that for convergence of voltages at 230 V (grid voltage) to occur the starting dq current values must be relatively close to the final dq current values. Thus to allow evaluation of the PMSG at torque values below 0.5 p.u. step 2 in the above method must be modified to allocate some portion of I_s to I_{ds}.

5.4 Optimisation of PMSG

The PMSG is optimised using the *VisualDoc* optimisation suite. To determine the operating point the FE simulations are run using *SEMFEM*, a custom in-house FE package, along with a script facilitating the iterative process described in Section 5.3. The optimisation is done by manipulating input variables for the FE package, and then evaluating the output of the FE package until an optimum is reached. This process is illustrated in Fig. 5.3. The input variables used during the optimisation process are shown in Fig. 5.4 and given in Table 5.1. The objective function chosen for the optimisation is active mass, which is minimised, while all other output parameters are subject to constraints, with these constraints given in Table 5.2.

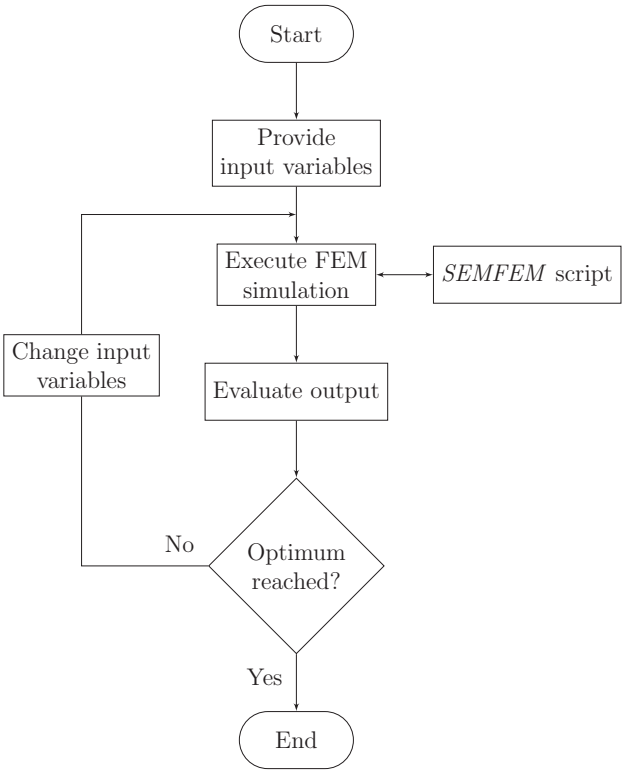

Figure 5.3: Flow diagram of the *VisualDoc* optimisation process

The input variables of the optimisation are all dimensions of the PMSG, with the exception of rated copper losses P_{cus} and number of turns N_c. It is necessary to include N_c as an optimisation input since the internally generated voltage varies depending on the dimensional variables, and N_c needs to be

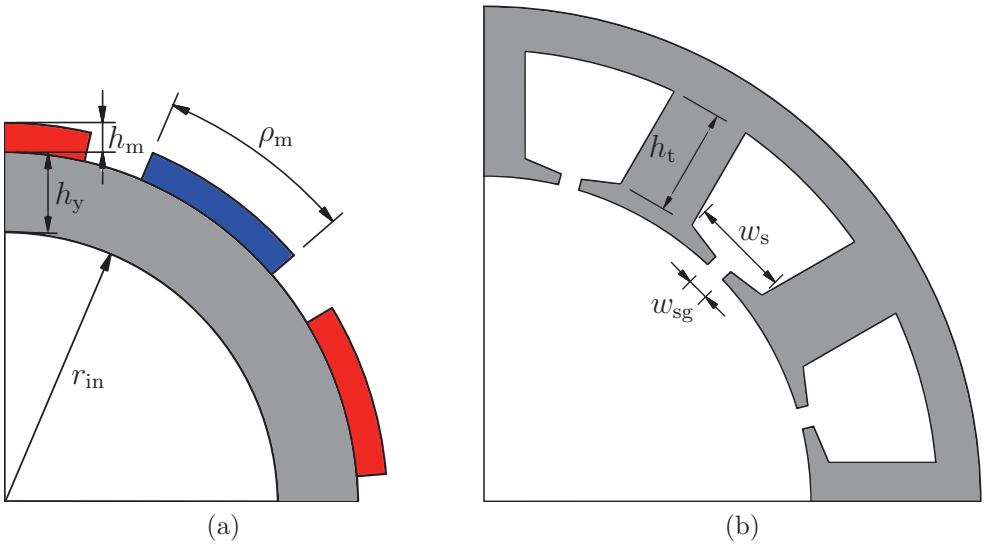

Figure 5.4: Dimensions used as optimisation input variables

adjusted accordingly to ensure the internally generated voltage roughly matches the grid voltage, since the grid voltage always remains constant. Also note that, since a gradient-based optimiser is used, N_c must be represented in the optimisation suite as a real number, but is rounded to the nearest integer in the FE package, since N_c is an integer.

5.5 Optimisation Results

The optimisation is done using the MMFD (modified method of feasible direction) algorithm. The optimised input variables are given in Table 5.1, as well as the minimised objective function, the active mass.

The active mass is optimised to be less than 10 kg, but this excludes the rotor shaft, end windings or any other external mounting fixtures. The magnet mass is just over 700 g, which is relatively low, along with a magnet height of 4.6 mm. The machine has a fixed outer radius of 92.5 mm, since it is intended that the generator should be built into the casing of an existing motor. The short axial stack length of 77 mm gives an aspect ratio of 2.4:1 (diameter to length), making the machine quite short.

The final values of the parameters constrained during the optimisation are given in Table 5.2, with the constraint limits also shown. All constraints were

Table 5.1: Design variables and optimised values for PMSG

Fixed Input	**Value**
Synchronous Speed	600 rpm
Outside Radius	92.5 mm
Optimisation Variables	**Optimised Value**
Axial Length - l_a	77 mm
Slot Width - w_s	18.5 mm
Slot Gap Width - w_{sg}	21.8% of w_s (4 mm)
Tooth Height - h_t	20 mm
Magnet Pitch - ρ_m	72.8% of pole pitch (26.2°)
Magnet Height - h_m	4.6 mm
Rotor Yoke - h_y	12.5 mm
Inside Radius - r_{in}	42.9 mm
Number of Turns - N_c	145
Rated Copper Losses - P_{cus}	130 W
Objective Function	**Optimised Value**
Active Mass (minimised)	9.92 kg

Table 5.2: Optimisation constraints

Constraint	**Limits**	**Values**
Generated Torque	36 Nm $< T <$ 38 Nm	36.57 Nm
Torque Ripple	$< 9\%$	9%
Efficiency	$> 93\%$	93%
Real Power Output	$>$ 2140 W	2141 W
Rated Power Factor	> 0.9	0.9767
Current Density	$<$ 5.5 A/mm^2	4.84 A/mm^2

met sufficiently, although it must be noted that the torque ripple, real power output and efficiency were all very close to their constraint limits. This was largely due to the torque ripple which was noticeably difficult to get below 12% without sacrificing efficiency, and thus ultimately power output.

5.6 Chapter Summary

The grid-connected PMSG is designed using FE simulations in combination with the *VisualDoc* optimisation suite. The operating point of the PMSG is determined using an iterative method to determine the voltage and current phasors, since the terminal voltage is fixed to the grid voltage. The iterative method is facilitated using *dq* equivalent circuit models. Performance calcula-

tions are also done using *dq* equivalent circuit models. A near optimal machine is designed with a rated torque of 36.57 Nm, efficiency of 93%, power output of 2141 W ($\approx$ 2.2 kW) and power factor of 0.977. It is noted that the 10/12 pole/slot combination seems to exhibit high amounts of torque ripple. In this case the torque ripple was limited to 9%, however it was found that it was quite difficult to attain a value lower than 12%, and the optimisation required several sessions with varying starting points to attain a 9% torque ripple.

Chapter 6

Calculated and Measured Results

The proposed drive train is evaluated by considering a combination of simulated and measured results, as well as some results derived from measured and calculated values. The results are presented in the same order as the chapters in this thesis, first looking at the gearbox, then the slip coupler and finally the PMSG. As mentioned earlier, special attention is given to the slip coupler and the measured results attained from the slip coupler prototype.

6.1 Gearbox Measurements

The gearbox is evaluated first, since it is of great importance that the efficiency characteristic of the gearbox over its entire load range be known. This is due to the test set-up used for the slip coupler. The slip coupler is mounted directly on the output shaft of the gearbox, thus there is no space to insert a torque sensor between the gearbox and slip coupler. Consequently the output speed and torque of the gearbox must be calculated from its input speed and torque.

6.1.1 Gearbox Test Set-up

The gearbox test set-up, as is detailed in Chapter 3, is repeated here for convenience. The set-up is driven by a large 55 kW induction motor, which runs through the gearbox and is connected to a DC machine which is run as a generator. The DC machine is gradually loaded up via external resistors

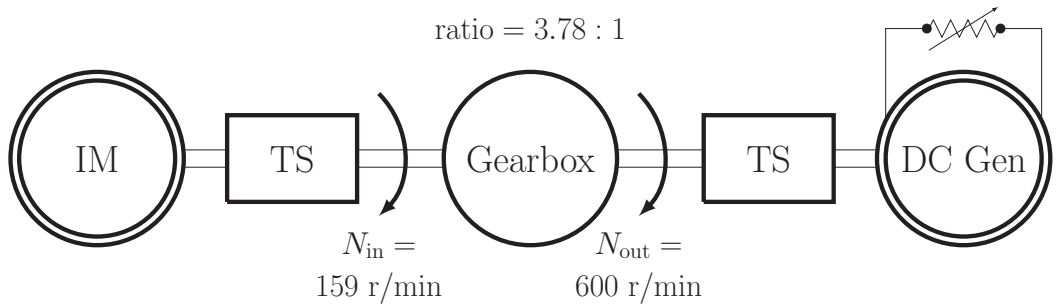

(a)

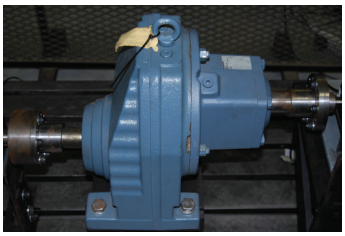

(b)

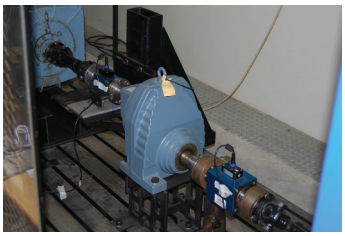

(c)

(d)

Figure 6.1: The gearbox test set-up, (a) illustrated with a diagram, and also shown by photos in (b) - (d).

to enable testing of the gearbox over its entire load range. The test set-up is shown in Fig. 6.1, along with pictures of the actual test bench used.

Torque sensors are placed on both sides of the gearbox, which allows for the calculation of efficiency. Note that both torque sensors measure with a percentage error (specified as 0.5% of sensor rated torque). These measurements, along with their errors, are multiplied when calculating derived values, such as efficiency. Consequently the percentage error also multiplies, which can greatly reduce overall accuracy. To counteract this the measurements are repeated several times on different dates, to ensure that representative sample data is recorded. The mean of this data set is then assumed to be the actual performance of the gearbox.

6.1.2 Gearbox Test Results and Characterisation

The measured results of the gearbox testing are given and discussed in Chapter 3, but it is also required that a curve be fitted onto the data points, to allow for

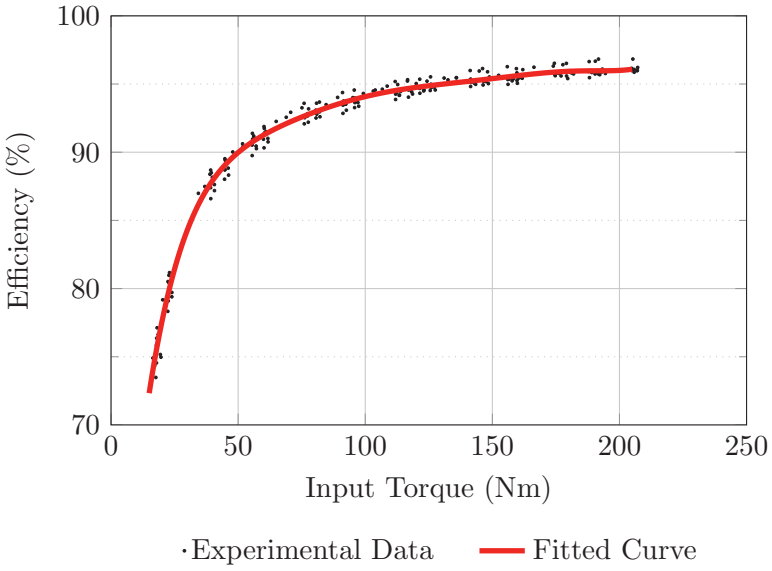

Figure 6.2: Experimental results of gearbox tests, with a 7th order polynomial curve fitted onto the data.

easy calculation of gearbox efficiency, based on any given value for input torque. To this end a simple least squares method is used to fit a 7th order polynomial onto the measured data points. The fitted curve is shown in Fig. 6.2, and is seen to be a good estimation of the actual data.

The fitted curve can be written in terms of input torque (T_{in}) and gearbox efficiency (η_{gb}) as

$$\begin{aligned}\eta_{\text{gb}} =&(1.485 \times 10^{-15})T_{\text{in}}^7 - (1.307 \times 10^{-12})T_{\text{in}}^6 + (4.775 \times 10^{-10})T_{\text{in}}^5 \ldots \\ &- (9.381 \times 10^{-8})T_{\text{in}}^4 + (1.073 \times 10^{-5})T_{\text{in}}^3 - (7.233 \times 10^{-4})T_{\text{in}}^2 \ldots \\ &+ (0.0277)T_{\text{in}} + 0.439. \end{aligned} \tag{6.1}$$

The efficiency curve allows for the calculation of the gearbox efficiency for any given input torque. Thus if a torque sensor is placed on the input side of the gearbox, the readings from the torque sensor can be used to calculate the output power of the gearbox.

Additionally, the gear ratio, taken as the average recorded ratio between input and output speeds of all experimental data points, was found to be 3.775, in line with the manufacturers' specifications. The output speed can be calculated by multiplying the input speed with the ratio of 3.775.

Thus with output speed and output power known, the output torque can also be calculated. This means that all output values of the gearbox can be

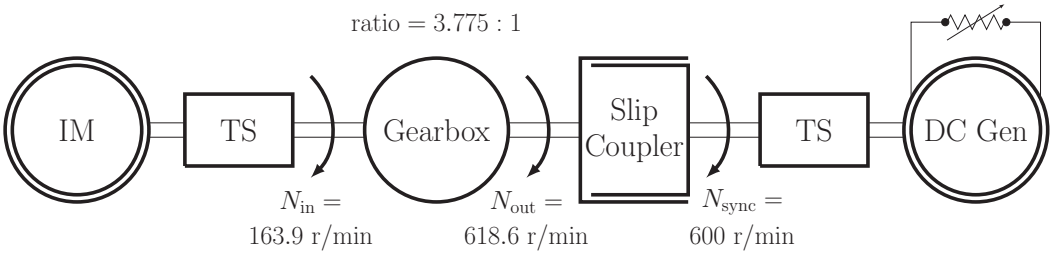

Figure 6.3: Diagram illustrating the slip coupler test bench set-up.

calculated with only the input values known. This is very useful, since this allows us to calculate the input values of the slip coupler without the need of a torque sensor between the gearbox and slip coupler.

6.2 Slip Coupler Results

The slip coupler is the main focus of this study, and positive test results are of great importance to prove the feasibility of such a free standing S-PMC. Trouble is taken to ensure that measured results of the slip coupler prototype are attained, and that these are in line with the simulated results.

6.2.1 Slip Coupler Test Setup

The slip coupler test set-up is very similar to that of the gearbox test set-up, with only the slip coupler prototype added to the system. The slip coupler test set-up is depicted in Fig. 6.3. As mentioned earlier, the slip coupler is directly mounted on the output shaft of the gearbox, with the slip coupler input values calculated using (6.1) and the measured values of the torque sensor on the left hand side of Fig. 6.3. The slip coupler output values are measured using the torque sensor on the right hand side. The tests are performed in a similar fashion to the gearbox tests where the DC generator is loaded up via external resistors to enable the evaluation of the slip coupler over its entire load range. Note that the output speed of the slip coupler is kept at a constant 600 r/min during all tests.

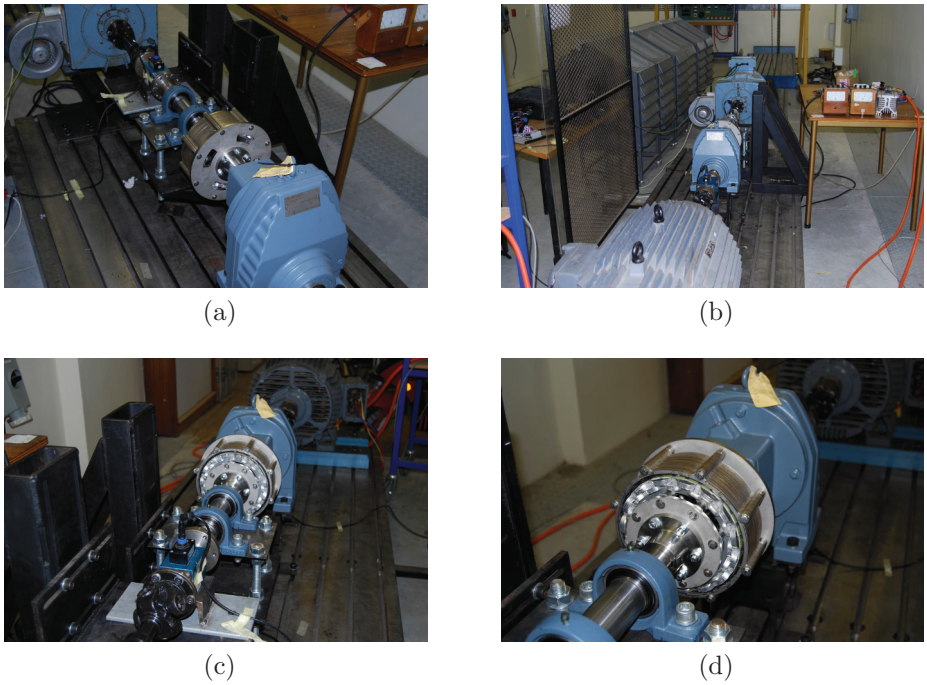

(a) (b)

(c) (d)

Figure 6.4: The slip coupler test bench with (a) the slip coupler mounted on the gearbox output shaft, (b) the drive induction motor, (c) the output side of the slip coupler and (d) a close up of the slip coupler output side connected to the shaft and bearing assembly.

Pictures of the actual test set-up used are shown in Fig. 6.4. Note that the output side of the slip coupler is mounted on a shaft and bearing assembly, which is included purely to help support the weight of the slip coupler. The other side of the shaft is connected to the output torque sensor.

Note that, as in the gearbox test set-up, the percentage error on the two torque sensors multiplies when calculating slip and efficiency. The measurements are made slightly more inaccurate by the fact that the slip coupler input values cannot be measured, but are calculated from the gearbox input values. Once again, to counteract this, large numbers of measurements are taken over several days of testing, and the average of the measured/calculated values are assumed to be representative of the actual values.

6.2.2 Slip Coupler Simulation and Test Results

The experimental results are compared to simulated results, to determine the validity of the FE model. These comparisons can only be made for the limited

variables which can be measured on the test bench, such as slip versus torque and slip versus efficiency. If the measured and simulated values agree quite well, it can be assumed that other simulated values are reasonable estimates of actual performance.

To further evaluate the slip coupler, simulated values are considered. The simulated values are primarily attained from the same time-stepped, static simulation used to optimise the machine. In this case an in-house FE package called *SEMFEM* is used. To verify the FE model, all static results are compared to the transient FE results obtained from running the same model on *Infolytica Magnet*. The transient results are a good way to verify the static results, since the transient simulation requires no input values besides input and output speeds to determine performance variables.

6.2.2.1 Thermal Considerations

The measured experimental results of torque versus slip are plotted along with the static and transient FE simulation results, as shown in Fig. 6.5a. The static and transient FE simulations match each other very closely, as can be seen in Fig. 6.5a, but the simulated results do not match the measured results; there is a clear difference in the gradients of the two datasets. At low slip values, as in this case, the gradient is almost entirely dependent on the resistance value of the conductors. This implies that the resistance values of the simulations are calculated incorrectly. When considering (A.10) it is clear that ρ_t is the only variable which can be incorrect, since the dimensional variables are calculated quite accurately. ρ_t was calculated with an estimated operating temperature of 75 °C, which is conventional for closed, low wattage machines. However, the slip coupler is an open machine, with much better heat dissipation capabilities than conventional closed induction machines.

Since it is clear that the operating temperature estimation of 75 °C is incorrect, a limited investigation is made into the thermal characteristics of the slip coupler. An infra-red image of the slip coupler is taken after running at full load for two hours, and is given in Fig. 6.6. From the image it is clear that the rotor laminations reach temperatures in excess of 30 °C, but the conductor end windings have a much lower temperature (±22 °C). This is somewhat puzzling, since the aluminium conductors are the only sources of heat on the rotor. The end windings are thus effectively cooled during rotation by the ambient room

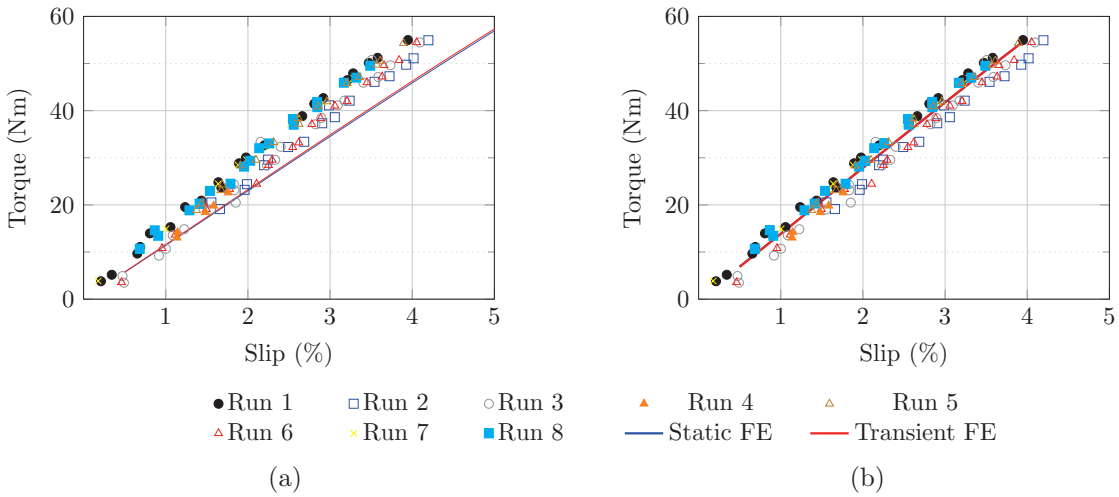

Figure 6.5: Measured and FE results of FE simulations run at (a) 75 °C and (b) 45 °C.

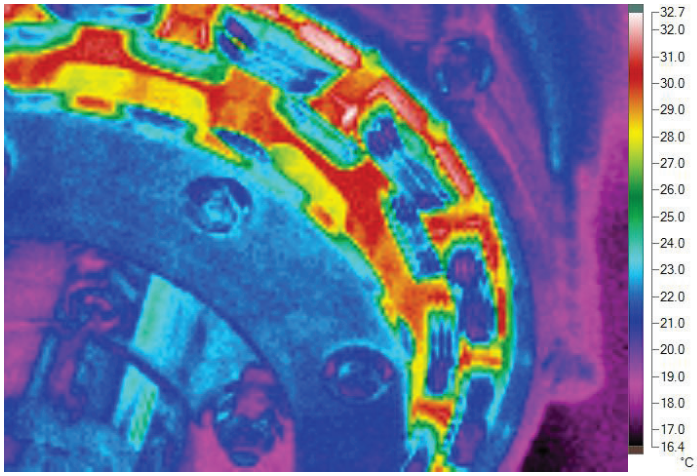

Figure 6.6: Infra-red image of slip coupler windings, after running at full load for two hours.

temperature, but the conductors in the stack must have a temperature in excess of 30 °C.

Unfortunately the temperature of the conductors in the stack cannot be measured without disassembling the machine. Thus the conductor temperature must be estimated by some method, knowing that the conductor temperature must lie somewhere between 32 °C and 75 °C. The conductor temperature is estimated by determining the rotor resistance from the measured conductor losses, and the effective temperature from the rotor resistance.

From prototype measurements the conductor losses are found to be around 80 W. It is assumed that the ratio between upper and lower layer conductor losses remain constant, independent of temperature, which is a reasonable assumption since the ratio matches to within three decimal places when evaluated at 20 °C and at 75 °C. Further, the conductor RMS current must lie somewhere between the current values of the 20 °C and 75 °C simulations. An initial guess for the operating current is made by taking the average of the 20 °C and 75 °C simulation currents. This is found to be $(223.5 + 181.7)/2 = 202.6$ A. Using the current estimate, the ratio between the upper and lower layer conductor losses and (4.19), values for upper and lower layer conductor resistances are determined. Using either of these, along with (A.10) and (A.11), a conductor operating temperature of 45 °C is calculated.

An FE simulation is run using this new temperature value, and the simulated losses compared with the measured losses. If the losses do not match, the conductor current is adjusted upwards or downwards as required until the losses match. In this case it is found that a conductor operating temperature of 45 °C produces conductor losses of 79 W in the FE simulation, which is very close to the measured value of 80 W. It is thus assumed that the slip coupler conductors run at 45 °C at rated conditions.

A new set of FE simulations are run for various slip values, all at 45 °C. The slip versus torque characteristics of these simulations are shown in Fig. 6.5b, and are in agreement with the measured data.

6.2.2.2 Final Results

The updated slip coupler simulations are compared with the measured prototype values. This is done for torque versus slip and efficiency versus slip. The results are shown in Fig. 6.7. As can be seen, the measured results agree relatively well with the simulated results. There is a degree of noise present in the measured values, but this is due to the sensor inaccuracy mentioned earlier. The variance is slightly more pronounced for Fig. 6.7a, since both efficiency and slip must be derived from values measured from both torque sensors, thereby compounding the measurement error.

The efficiency, as shown in Fig. 6.7a, decreases linearly with an increase in slip, as is to be expected. The efficiency of the slip coupler is 97% at a rated slip of 3%. The torque, as given in Fig. 6.7b, increases linearly with

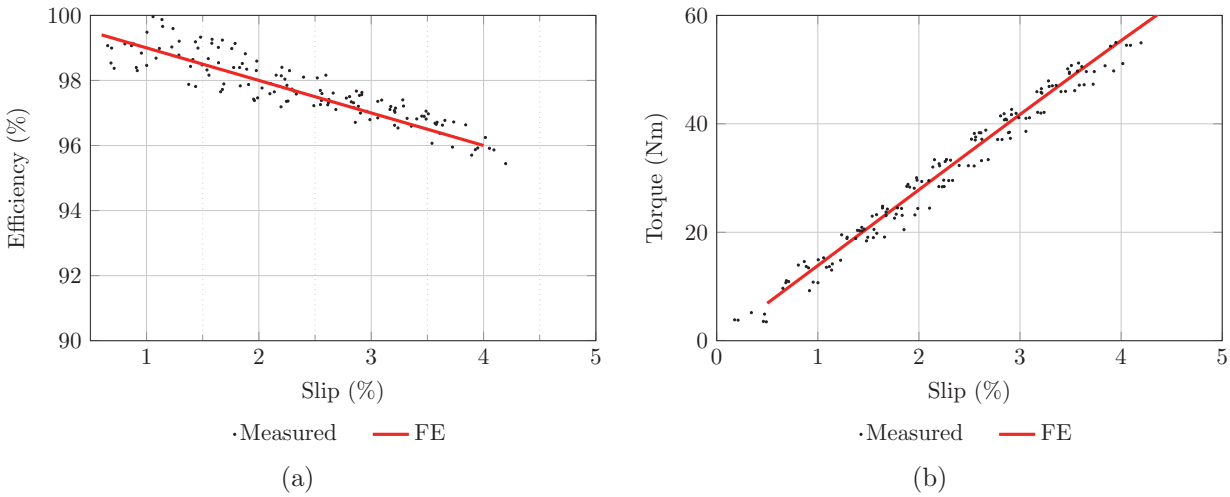

Figure 6.7: Measured and FE results of (a) efficiency and (b) torque versus slip.

an increase in slip, which is also to be expected for low slip values. The slip coupler transfers about 42 Nm of the torque at a rated slip of 3%, which is slightly higher than the initial design. This difference is due to the incorrect temperature value used in the initial simulations, as explained earlier.

Several other slip coupler metrics are also of interest, such as the flux linkage, current and torque waveforms, as well as the breakdown (maximum) torque of the slip coupler. These metrics could not be measured with the test set-up used in this investigation, but the FE values for both static and transient simulations are given, as shown in Fig. 6.8. In all cases the static and transient simulation values agree quite well.

The current amplitudes, as shown in Fig. 6.8b, are quite high, with the upper layer current in excess of 300 A. This is due to the large conductor areas, as well as the fact that the conductors only have one turn. However, the current density is still very low (less than 3 A/mm^2). Also note the clear difference in current amplitudes between the upper and lower layer coils in Fig. 6.8b, which necessitates the use of the analysis method described in Section 4.2.

The torque waveform, given in Fig. 6.8c, is shown to be very stable with very little torque ripple present, which is due to the 28/30 pole/slot combination used. Torque over a large slip range is shown in Fig. 6.8d, with a high breakdown torque value of 3.4 p.u. (144 Nm). Additionally, it can be noted that the slip coupler prototype can operate continuously above rated conditions, provided that the current density does not exceed 5.5 A/mm^2.

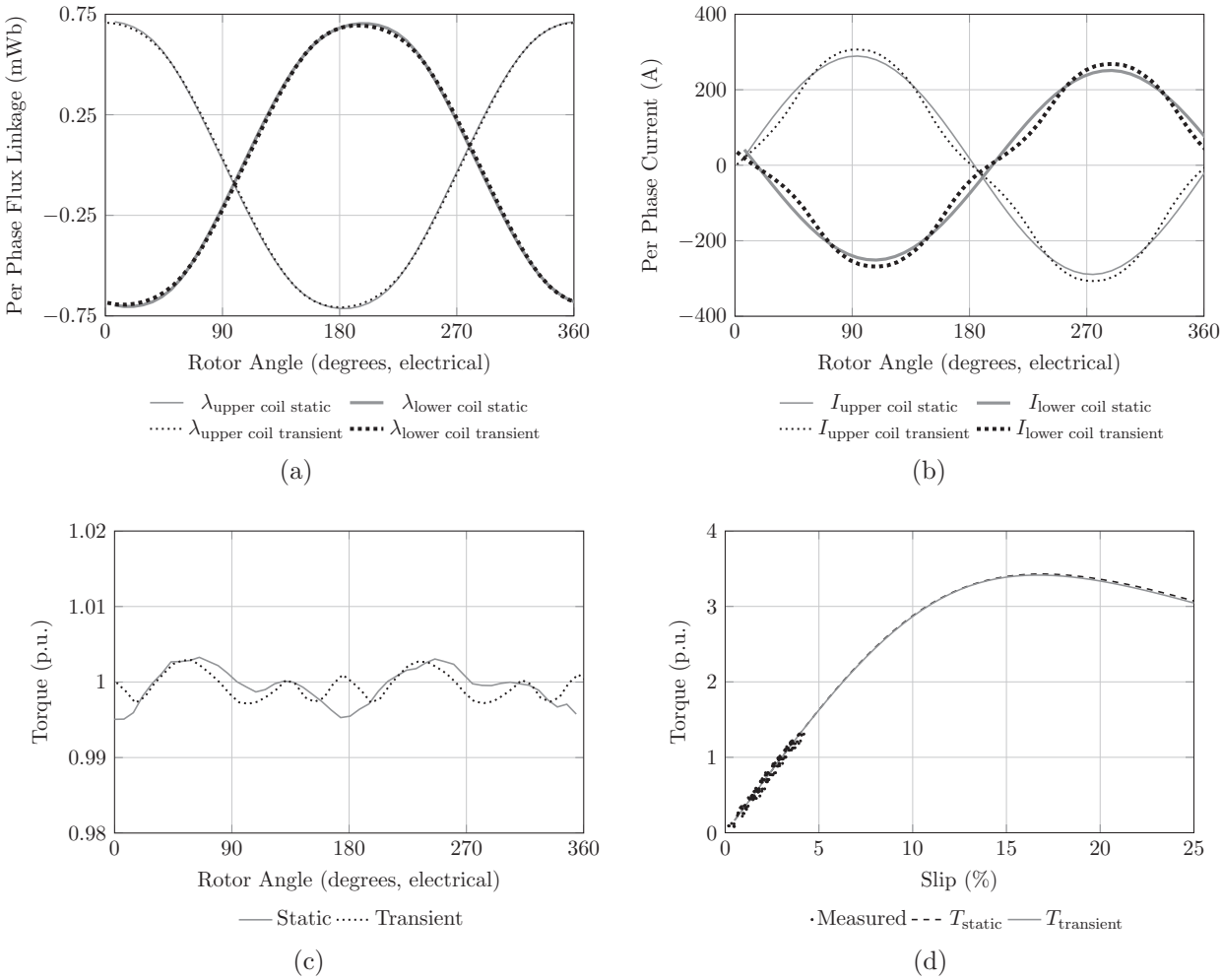

Figure 6.8: FE simulated metrics for the slip coupler, with (a) flux linkage, (b) current, and (c) torque waveforms shown. (d) Slip versus torque over a large slip range is also given.

6.3 PMSG Simulation Results

The construction of a PMSG prototype falls outside of the scope of this investigation, and thus only FE simulation results are given. The PMSG FE model is simulated using static, time stepped FE simulations, once again using the in-house package *SEMFEM*. These static simulations are verified against transient FE simulations run on *Infolytica Magnet*, to ensure that the FE model is constructed correctly. A series of simulations are run on both packages, over the expected operating range of the PMSG, with the same input current magnitudes and current angles used for both packages. The set of

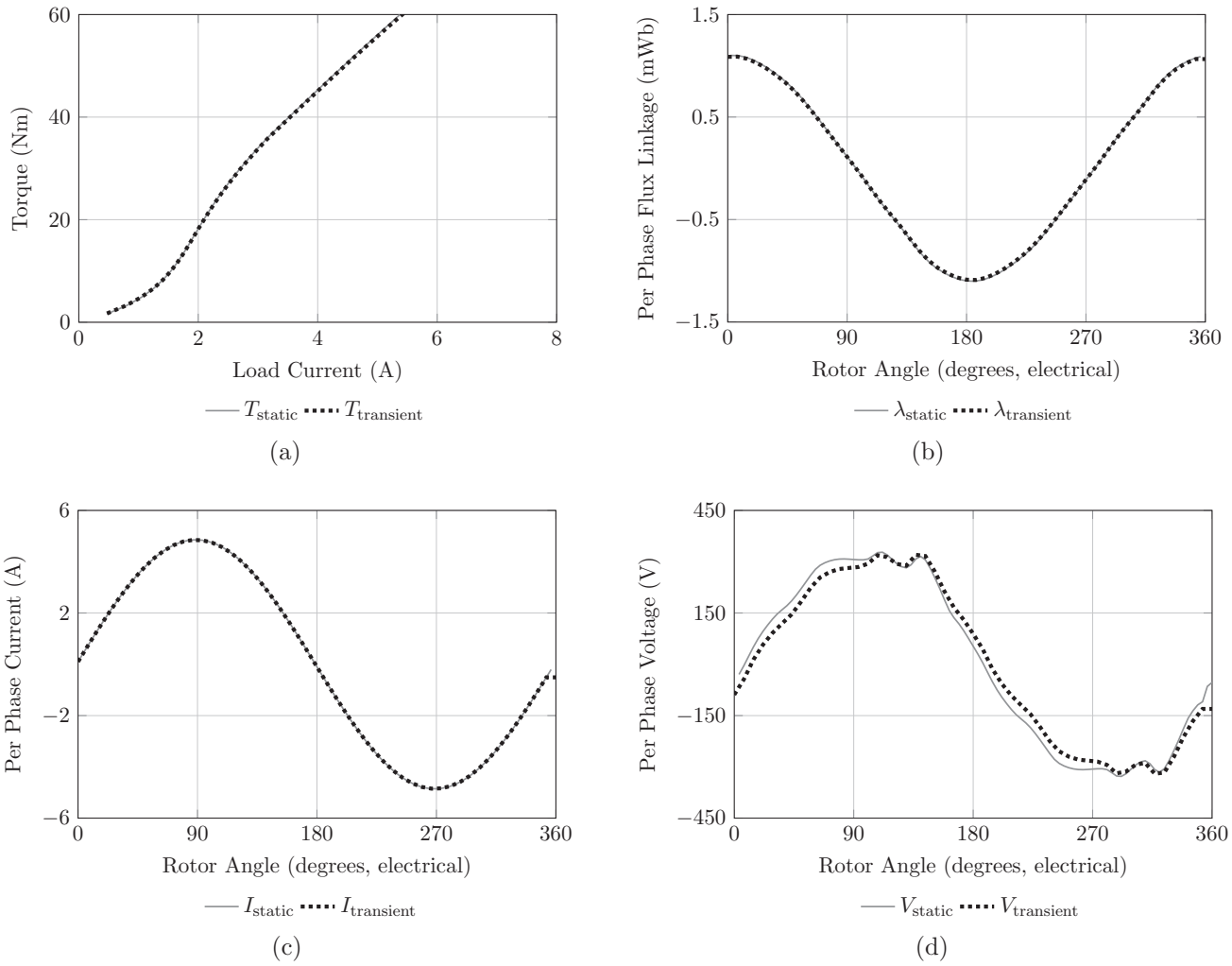

Figure 6.9: Comparison of static and transient FE results, with (a) torque versus RMS load current, (b) per phase flux linkage, (c) per phase current and (d) phase voltage.

current magnitudes and angles are determined using the method described in Section 5.3. Note that the transient simulation requires current magnitudes and angles as input, since a fixed speed transient simulation of a grid-connected synchronous machine cannot determine the current phasors by itself, unlike a similar simulation of an induction machine.

The flux linkage, voltage and current waveforms as well as torque versus load current of the two simulations are compared, and shown in Fig. 6.9. All of these results compare quite well between the static and transient simulations.

The rated input torque of 36.6 Nm results in an RMS load current of 3.25

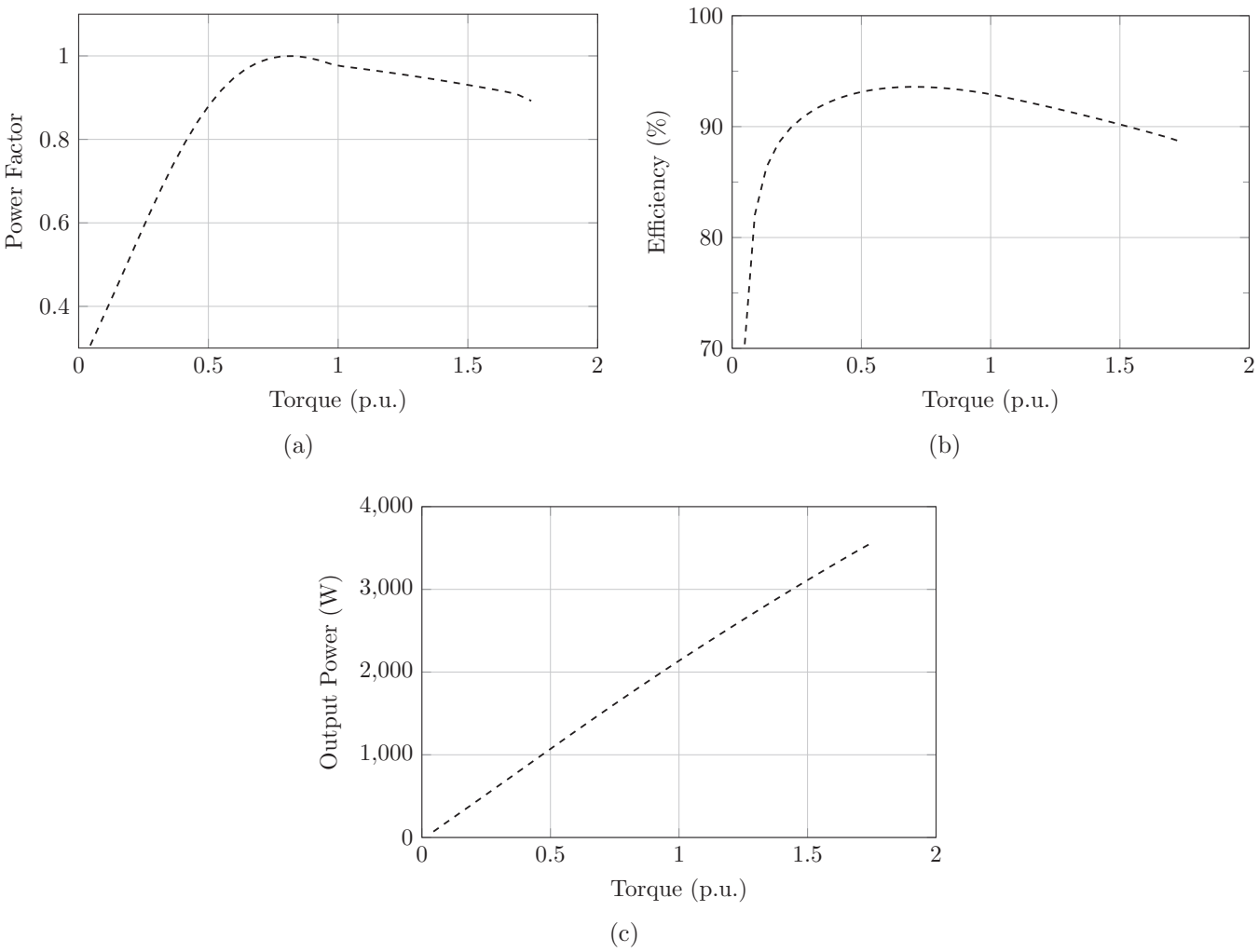

Figure 6.10: FE simulated PMSG metrics, with (a) power factor versus input torque, (b) efficiency versus input torque and (c) output power versus input torque.

A, as shown in Fig. 6.9a, which is thus the rated current of the PMSG. The peak phase voltage value of the PMSG is shown to be very close to 325 V, as shown in Fig. 6.9d, which implies an RMS phase voltage of 230 V, which is the required voltage to enable direct grid connection.

The simulated power factor, efficiency and output power versus input torque of the PMSG are also of interest, and are given in Fig. 6.10. The power factor is shown to be between 0.97 - 0.98 at rated torque, which is quite favourable, and remains above 0.9 for most feasible loads above rated load. At torque values below 0.4 p.u. (15 Nm) the power factor is quite poor, and rapidly falls from 0.8 to below 0.4. The PMSG efficiency, as shown in Fig. 6.10b, is above 85%

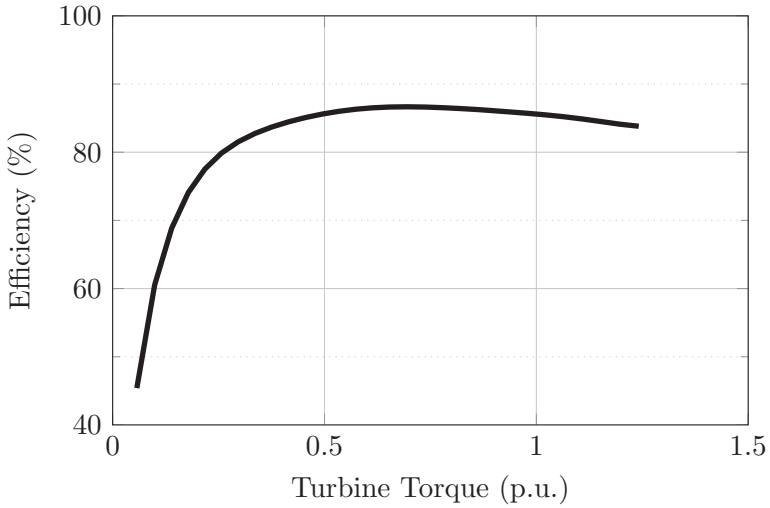

Figure 6.11: Efficiency versus input torque for the entire drive train.

for all input torque values above 0.15 p.u. (5 Nm), which is quite favourable. The PMSG has an efficiency of 93% at rated load, which is relatively good for such a small generator, but this high efficiency can mostly be attributed to the use of permanent magnets. The PMSG produces real output power of 2140 W at rated torque, which is very close to the designed power rating of 2200 W, and should easily be able to run at 2200 W.

6.4 Drive Train Efficiency

To evaluate the system as a whole, it is required that the efficiency of the entire system must be calculated. This is done using a combination of measured and simulated results to calculate the system efficiency versus input torque over the expected load range. The result can be seen in Fig. 6.11. The efficiency is initially low, with values below 70% for input torque values below 0.15 p.u. (25 Nm). However, above 0.15 p.u. the efficiency rises rapidly to above 80%, and can be seen to be above 85% for most of its load range. The efficiency at rated load (165 Nm) is 85.5%, which is quite reasonable. The efficiency remains relatively high up to a torque value of 1.25 p.u. (200 Nm), with no data available for higher values.

6.5 Chapter Summary

In this chapter it is shown that a small scale commercial down speed gearbox can be run in the reverse direction, with an efficiency of up to 96%. The slip coupler prototype is shown to agree very well with the FE simulations, after adjustments for temperature are made. The slip coupler performed as expected, with a very high efficiency, low operating temperatures and a breakdown torque value of more than three times the rated torque. The PMSG simulations indicate that the PMSG design could potentially be used in conjunction with the rest of the system for direct grid-connected power generation. The PMSG has a good efficiency of 93% at rated conditions, and produces 2140 W of output power. The PMSG power factor is also favourable, with generally high values, and a value above 0.97 at rated conditions. Finally, the overall system efficiency is shown to be in excess of 80% over most of the load range, with an efficiency at rated conditions of 85.5%.

Chapter 7

Conclusions and Future Work

The investigation of the proposed drive train, including gearbox, slip coupler and PMSG, is completed. An investigation into wind site statistics is done to determine the near-optimal operating speed range of the proposed drive train. The gearbox is tested and characterised to determine its efficiency over a large load range. A slip coupler prototype is designed, optimised, constructed and tested in the laboratory, with good results achieved. A PMSG prototype is designed and optimised, but not built, and the simulation data is used to enable evaluation of the entire drive train. The drive train as a whole is evaluated in terms of efficiency, using simulated and measured values.

7.1 Conclusions From Research

The following conclusions are drawn from the research:

- Using a Weibull curve fitting and basic statistics to determine turbine power yield appears to be an effective method of turbine speed and generator size selection, and allows for selection of an optimal or near optimal fixed turbine speed for any site, given that the wind site data and turbine C_p curve are available.
- A small down-speed gearbox can be run in the reverse direction as an up-speed gearbox. The gearbox in this investigation was only tested for about 50 hours, and long term field testing is an aspect that requires further investigation. It could possibly be feasible to use such a gearbox for wind generator drive train applications, but this remains to be proven.

The gearbox achieves a high efficiency in the reverse direction, with an efficiency of 96% at rated loads. It must be noted that the gearbox must first reach steady state operating temperature for these efficiencies to be achieved.

- A free standing S-PMC, such as the slip coupler, is a feasible concept and it has been proven that it works very well in terms of efficiency and torque transfer. The design is also quite simple, with flat magnets used, as well as stacked aluminium plates for coils, which makes construction fairly simple.

- The slip coupler displayed superior thermal properties, with a much lower actual operating temperature than initially estimated. This is due to the open design and rotating coils, which allow the end windings of the machine to cool very effectively while rotating. This is in contrast to conventional closed machines, where the end windings are enclosed at the end sections and reach very high temperatures due to poor air circulation. The open design potentially makes the slip coupler more vulnerable to the elements, but it is expected that during field operation the nacelle housing of a turbine should provide sufficient protection. The housing enclosure may result in slightly higher operating temperatures for the slip coupler, depending on the design of the housing. For the test conditions in this study the superior thermal properties imply that a considerably smaller prototype can be used to achieve the original design torque of 35 Nm.

- The analysis method used to model and optimise the slip coupler with time-stepped, static FE simulations is shown to be effective, and compares favourably with the same machine simulated using transient simulations. The measured results from the slip coupler prototype also compare favourably to the static FE simulation results, thereby further validating the method.

- The simulated PMSG appears to be a feasible machine for direct grid-connected operation. The PMSG also has a good power factor and efficiency for such a small machine, and it is envisioned that efficiencies in excess of 94% can be achieved for larger machines.

- The proposed drive train as a whole, when considering the measured and simulated results, appears to be feasible. The drive train can be used for a geared, direct grid-connected wind turbine system, and has a good overall efficiency of above 80% for most of its operating range.

7.2 Future Work

Since only measured results of the gearbox and slip coupler were taken, some areas for future work still exist:

- Construction and lab testing of the designed PMSG prototype would add value to the investigation, and allow for measured evaluation of all components in the drive train.
- Laboratory testing, and eventually field testing of the entire drive train would provide measured results of the drive train as a whole, which will verify if the drive train can be used for direct grid-connected operation.
- FE thermal analysis during slip coupler design and optimisation could be very advantageous in reducing machine size, and should be considered in future prototype designs.
- Due to radial forces caused by the permanent magnets in the slip coupler, alignment is very difficult without using a hub assembly. The hub adds weight and complexity, and additional components that may fail. It is thus warranted to investigate whether the slip coupler can be mounted, aligned and operated without the need of a hub assembly.

List of References

[1] J. A. Baroudi and V. Dinavahi, "A Review of Power Converter Topologies for Wind Generators," in *Proc. IEEE International Electric Machines & Drives Conference (IEMDC 2005)*, San Antonio, Texas, USA, 2005, pp. 458–465.

[2] A. J. G. Westlake, J. R. Bumby, and E. Spooner, "Damping the power-angle oscillations of a permanent-magnet synchronous generator with particular reference to wind turbine applications," *IEEE Proceedings - Electric Power Applications*, vol. 143, no. 3, pp. 269–280, 1996.

[3] S. Grabic, N. Celanovic, and V. A. Katic, "Permanent magnet synchronous generator cascade for wind turbine application," *IEEE Transactions on Power Electronics*, vol. 23, no. 3, pp. 1136–1142, 2008.

[4] C. Rossi, P. Corbelli, and G. Grandi, "W-CVT Continuously Variable Transmission for Wind Energy Conversion System," in *Proc. IEEE Power Electronics and Machines in Wind Applications (PEMWA 2009)*, Lincoln, Nebraska, USA, 2009, pp. 1–10.

[5] T. Fukami, K. Nakagawa, Y. Kanamaru, and T. Miyamoto, "A technique for the steady-state analysis of a grid-connected permanent magnet induction generator," *IEEE Transactions on Energy Conversion*, vol. 19, no. 2, pp. 318–324, 2004.

[6] J. H. Potgieter and M. J. Kamper, "Design of new concept permanent magnet induction wind generator," in *Proc. IEEE Energy Conversion Congress and Exposition (ECCE 2010)*, Atlanta, Georgia, USA, Sep. 2010, pp. 2403–2408.

[7] ——, "Design of New Concept Direct Grid-Connected Slip-Synchronous Permanent-Magnet Wind Generator," *IEEE Transactions on Industry Applications*, vol. 48, no. 3, pp. 913–922, May 2012.

[8] ——, "Optimum design and technology evaluation of slip permanent magnet generators for wind energy applications," in *Proc. IEEE Energy Conversion Congress and Exposition (ECCE 2012)*, Raleigh, North Carolina, USA, Sep. 2012, pp. 2342–2349.

[9] ——, "Optimum Design and Comparison of Slip Permanent-Magnet Couplings With Wind Energy as Case Study Application," *IEEE Transactions on Industry Applications*, vol. 50, no. 5, pp. 3223–3234, Sep. 2014.

[10] A. Wallace, "A permanent-magnet coupling with rapid disconnect capability," in *Proc. IET International Conference on Power Electronics Machines and Drives (PEMD 2002)*, vol. 2002, Bath, UK, 2002, pp. 286–291.

[11] R. Hornreich and S. Shtrikman, "Optimal design of synchronous torque couplers," *IEEE Transactions on Magnetics*, vol. 14, no. 5, pp. 800–802, Sep. 1978.

[12] G. S. Highfill and L. A. Halverson, "Lowering total cost of ownership with breakthrough magnetic torque transfer technology," in *Proc. IEEE Cement Industry Technical Conference (2006)*, Phoenix, Arizona, USA, 2006, pp. 217–231.

[13] S. A. Akdag and A. Dinler, "A new method to estimate Weibull parameters for wind energy applications," *Energy Conversion and Management*, vol. 50, no. 7, pp. 1761–1766, Jul. 2009.

[14] J. Seguro and T. Lambert, "Modern estimation of the parameters of the Weibull wind speed distribution for wind energy analysis," *Journal of Wind Engineering and Industrial Aerodynamics*, vol. 85, no. 1, pp. 75–84, Mar. 2000.

[15] G. Masters, *Renewable and Efficient Electric Power Systems*, 1st ed. Chicester: John Wiley and Sons, 2004.

[16] J. Stegmann and M. Kamper, "Economic and efficient evaluation of different battery charging wind generator systems," in *Proc. Southern African*

Universities Power Engineering Conference (SUAPEC 2010), Johannesburg, South Africa, 2010, pp. 205–210.

[17] P. J. J. Van Wyk and M. J. Kamper, "Simplified Analysis Technique for Double Layer Non-overlap Multiphase Slip Permanent Magnet Couplings in Wind Energy Applications," in *Proc. IEEE International Electric Machines & Drives Conference (IEMDC 2015)*, Coeur D'Alene, Idaho, USA, May 2015, pp. 1317–1323.

[18] G. Renukadevi and K. Rajambal, "Generalized model of multi-phase induction motor drive using matlab/simulink," in *Proc. IEEE PES Innovative Smart Grid Technologies - India (ISGT 2011)*, Kerala, India, Dec. 2011, pp. 114–119.

[19] M. Sowmiya, G. Renukadevi, and K. Rajambal, "IFOC of five-phase induction motor drive," in *Proc. International Conference on Power, Energy and Control (ICPEC 2013)*, Dindigul, India, Feb. 2013, pp. 304–309.

[20] J. Pyrhonen, T. Jokinen, and V. Hrabovcova, *Design of Rotating Electrical Machines*, 1st ed. Chicester: John Wiley & Sons, 2008.

[21] M. J. Kamper, "Design Optimisation of Cageless Flux Barrier Rotor Reluctance Synchronous Machine," Phd, University of Stellenbosch, Stellenbosch, 1996.

[22] R. S. Miranda, "Current control of six phase induction motor under open phase fault condition," in *Proc. IEEE International Electric Machines & Drives Conference (IEMDC 2013)*, Chicago, Illinois, USA, May 2013, pp. 1391–1396.

[23] Wang Yu Lin, Liu Pin Kuan, Wu Jun, and Ding Han, "Near-Optimal Design and 3-D Finite Element Analysis of Multiple Sets of Radial Magnetic Couplings," *IEEE Transactions on Magnetics*, vol. 44, no. 12, pp. 4747–4753, Dec. 2008.

[24] Z. Mouton and M. J. Kamper, "Design of an eddy-current coupling for slip-synchronous permanent magnet wind generators," in *Proc. IEEE International Conference on Electrical Machines (ICEM 2012)*, Marseille, France, Sep. 2012, pp. 633–639.

[25] ——, "Modeling and Optimal Design of an Eddy Current Coupling for Slip-Synchronous Permanent Magnet Wind Generators," *IEEE Transactions on Industrial Electronics*, vol. 61, no. 7, pp. 3367–3376, Jul. 2014.

[26] V. B. Honsinger, "Theory of end-winding leakage reactance," *Power apparatus and systems*, vol. 78, no. 3, pp. 2–9, Aug. 1959.

[27] M. J. Kamper, A. J. Rix, D. A. Wills, and R. Wang, "Formulation, finite-element modeling and winding factors of non-overlap winding permanent magnet machines," in *Proc. IEEE International Conference on Electrical Machines (ICEM 2008)*, no. 3, Vilamoura, Portugal, Sep. 2008, pp. 1–5.

[28] N. Bianchi, S. Bolognani, M. Dai Pré, and G. Grezzani, "Design considerations for fractional-slot winding configurations of synchronous machines," *IEEE Transactions on Industry Applications*, vol. 42, no. 4, pp. 997–1006, 2006.

[29] J. H. J. Potgieter and M. J. Kamper, "Calculation Methods and Effects of End-Winding Inductance and Permanent-Magnet End Flux on Performance Prediction of Nonoverlap Winding Permanent-Magnet Machines," *IEEE Transactions on Industry Applications*, vol. 50, no. 4, pp. 2458–2466, Jul. 2014.

[30] F. W. Grover, *Inductance Calculations: Working Formulas and Tables*, 1st ed. New York: Dover Books, 1946.

[31] M. J. Kamper and F. S. Van der Merwe, "Influence of laminations on axially directed flux in induction motors," in *Proc. IEEE International Conference on Electrical Machines (ICEM 1988)*, May 1988, pp. 413–416.

[32] S. Sprague, "Lamination steels third edition," Electric Motor Education & Research Foundation, Tech. Rep., 2007.

[33] N. Bianchi and M. Dai Pré, "Use of Star of Slots in Designing Fractional-Slot Single-Layer Synchronous Motors," *IEE Proceedings - Electrical Power Applications*, vol. 153, no. 3, pp. 459–466, 2006.

[34] S. J. Chapman, *Electric Machinery Fundamentals*, 4th ed. New York: McGraw-Hill, 2005.

[35] S. D. Umans, *Fitzgerald & Kingsley's Electric Machinery*, 7th ed. New York: McGraw-Hill, 2014.

Appendices

Appendix A

Calculation of Machine Parameters

A.1 Calculation of End-Winding Leakage Inductance

Note: In all calculations given in the appendices metres (not millimetres) are used in the equations for the results to be correct. Elsewhere in this thesis the same variables are displayed and given in millimetres, for better readability.

A.1.1 Method 1

Several methods exist which can be used to calculate an estimated value for end-winding leakage inductance for a given machine. One of the methods used in this thesis is based on the work of Honsinger [26], which is based on classical boundary value equations of a three dimensional end coil surrounded on all sides by iron boundaries. The equations used here are close adaptations of the equations given in [26] and are given in [21]. Note that this method is intended for use with overlap, distributed windings, but is used in this case for non-overlap windings. The end winding leakage inductance is calculated (in henrys per phase) using:

$$L_{\mathrm{e}} = V_{(\mathrm{u})} N_{\mathrm{ph}} d_{\mathrm{i}} \left(\frac{2W k_{\mathrm{d}} k_{\mathrm{p(u)}}}{p} \right)^2 k_{\mathrm{e}(p)} \times 10^{-8} \quad (\mathrm{H}) \tag{A.1}$$

where

N_{ph} = Number of phases
d_{i} = Stator inner diameter (when calculating **stator** end winding inductance)
W = Number of turns in series per phase
k_{d} = Standard distribution factor (as calculated in Appendix B)
p = Number of poles

The values for $V_{(\text{u})}$ and $k_{\text{p(u)}}$ are dependent on the shape of the coil at the end winding. The shape is denoted by the subscript "u", where:

u = 1 for v-shaped end windings
u = 2 for elliptical shaped end windings
u = 3 for rectangular shaped end windings

$V_{(\text{u})}$ is a shape factor, and in the case of a double-layer winding configuration (as is used here), the values of $V_{(\text{u})}$ are given as:

$$V_{(1)}= 465 \quad V_{(2)} = 920 \quad V_{(3)} = 1040$$

$k_{\text{p(u)}}$ is an end winding pitch factor, and is calculated using:

$$k_{\text{p(1)}} = \frac{3\sin(\pi c_{\text{s}}/6q)}{4-(c_{\text{s}}/3q)^2} \tag{A.2}$$

$$k_{\text{p(3)}} = \sin(\pi c_{\text{s}}/6q) \tag{A.3}$$

$$k_{\text{p(2)}} \approx (k_{\text{p(1)}} + k_{\text{p(3)}})/2 \tag{A.4}$$

where c_{s} is the coil span, which is the coil pitch given in terms of the number of slots being spanned by a coil. q is the number of slots per pole per phase. Note that the equations for $k_{\text{p(u)}}$ above are also intended for overlap, distributed windings. Despite this reasonable values of $k_{\text{p(u)}}$ are attained for the PMSG ($\approx$ 0.92), but a very low value for $k_{\text{p(u)}}$ is attained for the slip coupler (≈ 0.4).

The final factor in the formula, $k_{\text{e}(p)}$, is an end winding factor, and is given in a figure in [26] for up to p (number of poles) = 10. $k_{\text{e}(p)}$ values for pole numbers greater than 10 had to be estimated or extrapolated from the data provided. The available and estimated values for $k_{\text{e}(p)}$ are given as:

$$k_{\text{e(2)}} = 0.51 \quad k_{\text{e(4)}} = 0.595 \quad k_{\text{e(6)}} = 0.64$$
$$k_{\text{e(8)}} = 0.785 \quad k_{\text{e(10)}} \approx 0.91 \quad k_{\text{e(28)}} \approx 3$$

The estimated value of $k_{e(p)}$ for $p = 10$ can be seen as more or less accurate, however the accuracy for $p = 28$ is a potential area for concern. Due to the unreasonable $k_{p(u)}$ values calculated for the slip coupler, as mentioned above, as well as the roughly estimated values for $k_{e(p)}$, it is decided that method 1 will not be used for this investigation, and an alternative method is explored.

A.1.2 Method 2

The second method used in this thesis is detailed in [29], and is derived from a combination of the the work done in [30] and [31]. This second method is determined by [29] to quite accurately reflect actual inductance values, and additionally can be used for non-overlap windings. Thus this method is used as the primary method to calculate end winding inductance in this thesis. The following equation is used to determine the per phase end-winding leakage inductance, without taking the effect of the lamination stack on the end-winding inductance into account:

$$L_{e(1)} = \frac{1.9739}{n_a^2}\left(\frac{2a^2}{b}\right) N_c^2 q_c K \times 10^{-6} \quad \text{(H)} \tag{A.5}$$

The next equation also calculates per phase end-winding leakage inductance, but this time takes the effect of the lamination stack into account:

$$L_{e(2)} = \frac{1.257}{n_a^2} l_e \left(\frac{2a}{b}\right) N_c^2 q_c K \times 10^{-6} \quad \text{(H)} \tag{A.6}$$

The value for K is calculated using $K = k_1 - k_2$, where k_1 is calculated as per below, and k_2 is attained from tables in [30], subject to dimensional variables a, b and c. The equation variables are defined as follows:

n_a = Number of parallel circuits
l_e = Length of end winding
N_c = Number of turns per coil
q_c = Number of coils per phase
p = Number of poles

These two equations are combined, as is explained in [29]. Two separate equations are possible for the two cases of $l_g \leq 2.5$mm, and $l_g > 2.5$mm, where l_g is the distance of the gap between the stack and the end winding.

$$L_e = L_{e(2)(l_e = w_t + 2w_c + 2l_g, b = 2w_c)} \text{ for } l_g < 2.5 \text{ mm} \tag{A.7}$$

$$L_{\mathrm{e}} = L_{\mathrm{e}(1)(l_{\mathrm{e}}=w_{\mathrm{c}}+2l_{\mathrm{g}},b=w_{\mathrm{c}})} + L_{\mathrm{e}(2)(l_{\mathrm{e}}=w_{\mathrm{t}}+w_{\mathrm{c}},b=2w_{\mathrm{c}})} \text{ for } l_{\mathrm{g}} > 2.5 \text{ mm} \tag{A.8}$$

where

w_{t} = Tooth width
w_{c} = Coil width
a = r_{c}
b = Varies as per (A.7) and (A.8)
c = h_{c}
r_{c} = Average coil radius, as measured from rotational axis
h_{c} = Coil height

To calculate k_1 the following equation is used:

$$k_1 = \frac{2\beta}{\pi}\left[\left(\ln\frac{4}{\beta} - \frac{1}{2}\right) + \frac{\beta^2}{8}\left(\ln\frac{4}{\beta} + \frac{1}{8}\right) - \frac{\beta^4}{64}\left(\ln\frac{4}{\beta} - \frac{2}{3}\right) - \frac{5\beta^6}{1024}\left(\ln\frac{4}{\beta} - \frac{109}{120}\right)\right] \tag{A.9}$$

where $\beta = b/2a$. (A.9) is a simplified (yet accurate) version of a series expansion, as per [30]. The simplification is explained in [29].

A.2 Calculation of Winding Resistance

A fairly straightforward formula for winding resistance is used, and is given in [21]. Note that this formula ignores the skin effect. The formula for per phase winding resistance (for either rotor or stator) can be written as:

$$R_{(\mathrm{r\ or\ s})} = \frac{2W\rho_{\mathrm{t}}(l + l_{\mathrm{e}})}{n_{\mathrm{a}}A_{\mathrm{co}}/z} \quad (\Omega) \tag{A.10}$$

where

W = Number of turns in series per phase
ρ_{t} = Resistivity of conductor at temperature t_{c} (see below)
l = Stack length
l_{e} = Length of end winding
n_{a} = Number of parallel circuits
A_{co} = Active conductor area of slot
z = Number of conductors per slot.

Table A.1: Resistivity and thermal coefficients for conductors

	1050A Aluminium	**98% IACS Copper**
Resistivity at 20 °C (ρ_{20})	2.82×10^{-8} Ω·m	1.759×10^{-8} Ω·m
Thermal Coefficient ($\mathrm{Y_t}$)	0.0043 $\mathrm{K^{-1}}$	0.0039 $\mathrm{K^{-1}}$

ρ_t is calculated using

$$\rho_\mathrm{t} = \rho_{20}(1 + \mathrm{Y_t}(t_\mathrm{c} - 20)) \tag{A.11}$$

where t_c is chosen to be 75 °C, as per convention. The conductor resistivity (ρ_{20}) and thermal coefficient ($\mathrm{Y_t}$) varies depending on the conductor material. The resistivity and thermal coefficients for the conductors used in this thesis are given in Table A.1.

A.3 Calculation of Core Loss and Core Loss Resistance

Core losses are calculated using a formula given in [21]. The following equation is used:

$$P_\mathrm{c} = \mathrm{C}f^\mathrm{x}(B_\mathrm{mt}^\mathrm{y}M_\mathrm{t} + B_\mathrm{my}^\mathrm{y}M_\mathrm{y}) \quad \mathrm{(W)} \tag{A.12}$$

where

C, x, y = Equation constants.
f = Fundamental frequency of varying flux (i.e. supply voltage)
B_mt = Maximum flux density in stator teeth
M_t = Mass of stator teeth
B_my = Maximum flux density in stator yoke
M_y = Mass of stator yoke.

B_mt, B_my, M_t and M_y are all attained from the FE package used during simulation. C, x and y are determined from loss-frequency curves for non-oriented silicon steel M400-50A, as given in [32]. The values for the constants are

$$\mathrm{C} = 0.0073 \quad \mathrm{x} = 1.3 \quad \mathrm{y} = 2.099.$$

With core losses calculated, the value of core loss resistance can also be calculated using:

$$R_{\mathrm{c}} = \frac{3E_{\mathrm{a}}^2}{P_{\mathrm{c}}} \tag{A.13}$$

where E_{a} is the RMS value of the internally generated voltage of the machine, given by

$$E_{\mathrm{a}} = \sqrt{\frac{(\omega_{\mathrm{s}}\lambda_{\mathrm{ds}})^2 + (\omega_{\mathrm{s}}\lambda_{\mathrm{qs}})^2}{2}}. \tag{A.14}$$

Appendix B

Calculation of Distribution Factor

The equations for the calculation of the distribution factor of the PMSG are given, using a formula for fractional slot machines as given by [33]. The distribution factor can be calculated using:

$$k_{\mathrm{d}} = \frac{\sin(\frac{q_{\mathrm{ph}}}{2} \cdot \frac{\alpha_{\mathrm{ph}}}{2})}{\frac{q_{\mathrm{ph}}}{2}\sin(\frac{\alpha_{\mathrm{ph}}}{2})} \text{ for } q_{\mathrm{ph}} \text{ even} \tag{B.1}$$

$$k_{\mathrm{d}} = \frac{\sin(\frac{q_{\mathrm{ph}}}{2} \cdot \frac{\alpha_{\mathrm{ph}}}{2})}{q_{\mathrm{ph}}\sin(\frac{\alpha_{\mathrm{ph}}}{4})} \text{ for } q_{\mathrm{ph}} \text{ odd} \tag{B.2}$$

where q_{ph} is the number of spokes (phasors that are combined to form a phase) per phase. α_{ph} is the angle between spokes. These are calculated using:

$$q_{\mathrm{ph}} = \frac{Q}{N_{\mathrm{ph}}t} \tag{B.3}$$

$$\alpha_{\mathrm{ph}} = \frac{2\pi}{Q/t} \tag{B.4}$$

with

Q = Number of slots
N_{ph} = Number of phases
t = Machine periodicity = Greatest common divisor $\{Q, p/2\}$
p = Number of poles